



Delft University of Technology

## The Influence of Parameterized Shallow Convection on Trade-Wind Clouds and Circulations in the HARMONIE-AROME Mesoscale Model

Savazzi, A. C.M.; Nuijens, L.; de Rooy, W.; Siebesma, A. P.

### DOI

[10.1029/2024MS004538](https://doi.org/10.1029/2024MS004538)

### Publication date

2025

### Document Version

Final published version

### Published in

Journal of Advances in Modeling Earth Systems

### Citation (APA)

Savazzi, A. C. M., Nuijens, L., de Rooy, W., & Siebesma, A. P. (2025). The Influence of Parameterized Shallow Convection on Trade-Wind Clouds and Circulations in the HARMONIE-AROME Mesoscale Model. *Journal of Advances in Modeling Earth Systems*, 17(2), Article 2024MS004538. <https://doi.org/10.1029/2024MS004538>

### Important note

To cite this publication, please use the final published version (if applicable). Please check the document version above.

### Copyright

Other than for strictly personal use, it is not permitted to download, forward or distribute the text or part of it, without the consent of the author(s) and/or copyright holder(s), unless the work is under an open content license such as Creative Commons.

### Takedown policy

Please contact us and provide details if you believe this document breaches copyrights. We will remove access to the work immediately and investigate your claim.



## RESEARCH ARTICLE

10.1029/2024MS004538

## Key Points:

- Parameterized shallow convection in the km-scale mesoscale model HARMONIE-AROME dampens mesoscale circulations
- Without parameterized shallow convection, stronger vertical motion, a larger heat flux and many smaller, yet deeper clouds develop
- Without parameterized momentum transport by shallow convection, cloudiness below the inversion and wind variance at mesoscales increase

## Correspondence to:

A. C. M. Savazzi,  
[a.c.m.savazzi@tudelft.nl](mailto:a.c.m.savazzi@tudelft.nl)


## Citation:

Savazzi, A. C. M., Nuijens, L., de Rooy, W., & Siebesma, A. P. (2025). The influence of parameterized shallow convection on trade-wind clouds and circulations in the HARMONIE-AROME mesoscale model. *Journal of Advances in Modeling Earth Systems*, 17, e2024MS004538. <https://doi.org/10.1029/2024MS004538>

Received 28 JUN 2024

Accepted 23 JAN 2025

# The Influence of Parameterized Shallow Convection on Trade-Wind Clouds and Circulations in the HARMONIE-AROME Mesoscale Model

A. C. M. Savazzi<sup>1</sup> , L. Nuijens<sup>1</sup>, W. de Rooy<sup>2</sup>, and A. P. Siebesma<sup>1,2</sup>

<sup>1</sup>Delft University of Technology, Delft, The Netherlands, <sup>2</sup>Royal Netherlands Meteorological Institute (KNMI), De Bilt, The Netherlands

**Abstract** Mesoscale numerical weather prediction models currently operate at kilometer-scale and even sub-kilometer-scale resolutions. Although shallow cumulus convection is partly resolved at these resolutions, it is still common to use a shallow cumulus parameterization (SCP). Within the context of the EUREC4A model intercomparison project, we evaluate how the modeled mesoscale cloud field in the trades responds to parameterized or explicit shallow convection in the mesoscale model HARMONIE-AROME. We simulate a region of  $3,200 \times 2,025 \text{ km}^2$  east of Barbados using a grid spacing of 2.5 km for a 2 months period (1 January to 29 February 2020). We compare three configurations of HARMONIE-AROME: (a) one with an active SCP (control), (b) one without parameterized momentum transport by shallow convection, and (c) one with an inactive SCP. The experiments produce different responses in the cloud field that are not incremental. With the SCP inactive, the model produces a warmer lower troposphere with many smaller but deeper clouds that precipitate more. Along with stronger resolved eddy kinetic energy, wider and stronger shallow meridional overturning circulations develop. In the configuration without parameterized momentum transport by shallow convection, the eddy-diffusivity scheme effectively takes over the missing transport in the sub-cloud layer up to  $\sim 800 \text{ m}$ . Above that level, horizontal wind variance increases as the total momentum flux decreases, enhancing eddy kinetic energy at scales of 2.5 km and larger. In contrast to the configuration with an inactive SCP, cloud top heights hardly deepen, but stratiform cloudiness below the inversion and mean cloud size increase.

**Plain Language Summary** Shallow cumulus clouds are important for the transport of heat, moisture, and winds in the lower 3–4 km of the atmosphere. Observations and high-resolution simulations show that over subtropical oceans, these clouds are coupled to atmospheric flows on mesoscales spanning a few to several hundred kilometers. These circulations help explain the horizontal clouds patterns, and thus their radiative impact on climate. Representing shallow cumulus clouds is challenging for models, as even a grid spacing of a few kilometers cannot resolve the narrow buoyant updrafts that sustain these clouds. Hence, a parameterization is often used to represent the transport by cumulus clouds on sub-grid scales. This study uses a mesoscale weather model to explore how turning off sub-grid transport of heat, moisture, and momentum affects clouds and mesoscale circulations. This is done to advance our conceptual understanding of the behavior of shallow cumulus clouds in current atmospheric models, and test how they are coupled to mesoscale circulations. The results show significant dependency of cloud organization and mesoscale circulations on the formulation of sub-grid shallow cumulus convection. When all sub-grid convection transport is removed, the model produces smaller, more numerous clouds that are stronger, deeper, and coupled to wider, stronger mesoscale circulations.

## 1. Introduction

Shallow cumulus clouds are widespread over tropical and subtropical oceans and small changes in their radiative effect, primarily through low cloud amount, have an important impact on modeled equilibrium climate sensitivity (ECS) (Bony, Schulz, et al., 2020; Schneider et al., 2017). In climate models, the vertical transport of momentum, heat and moisture by parameterized shallow convection has a strong control on low cloud amount and hence ECS (Vial et al., 2017). Recent observational evidence suggests that models might overestimate parameterized shallow convective transport and miss an important control on cloud amount, namely that of mesoscale circulations (Vogel et al., 2022). While in high-climate-sensitivity models lower-tropospheric mixing by shallow convection has a strong influence on (reducing) cloud-base cloudiness (Sherwood et al., 2014), observations show that

mesoscale motions have an equally important but opposite influence on lower-tropospheric humidity, whereby increased mesoscale overturning does not desiccate cloudiness (Vogel et al., 2022).

Current shallow convection parameterizations (SCPs) (Schlemmer et al., 2017) have been designed for models with a mesh  $\mathcal{O}(10\text{--}50\text{ km})$  and rely, among others, on the assumption that resolved (large scale) circulations and unresolved (turbulent) eddies are sufficiently distinct at these resolutions (Dorrestijn et al., 2013; Yu & Lee, 2010). However, in the past decades the mesh of mesoscale models has approached  $\mathcal{O}(1\text{ km})$ , at which scale current SCPs may no longer be valid and produce excessive fluxes (Honnert et al., 2011). Still, completely turning off the SCP at 1 km resolution, as often suggested in the literature (Bryan et al., 2003; Craig & Dornbrack, 2008; Petch et al., 2002), may not be appropriate when shallow convection is not fully resolved at that scale.

Wyngaard (2004) uses the term "terra incognita", while others have denoted sub-kilometer to km-scale resolutions as the "gray zone" of shallow convection (Honnert, 2019; Lancz et al., 2018), for which a few SCPs have been adjusted. Arakawa et al. (2011) suggest to follow a multi-scale modeling framework, with explicit representation of moist convection. Alternatively, they suggest to eliminate the assumption of small fractional area covered by convective clouds and then apply the parameterization to finer horizontal resolutions. Based on idealized large eddy simulations, Boutle et al. (2014) propose to suppress the non-local turbulence in the gray zone with a coefficient proportional to the ratio of grid mesh to boundary layer depth. Brast et al. (2018) test the scale adaptivity of mass-flux models, and Lancz et al. (2018) introduce a new closure for the SCP in which the initialization of the parameterized mass-flux depends on the horizontal resolution.

The debate on modeling shallow convection across the gray zone is ongoing, with one of the main challenges stemming from the wide range of scales involved in shallow convection organized on mesoscales. Atkinson and Wu Zhang (1996) describe the horizontal length scale of typical mesoscale shallow convection as ranging from a few kilometers to a few tens of kilometers. The rich mesoscale structure in cloud-topped boundary layers, such as cloud bands (LeMone et al., 1984; Malkus & Riehl, 1964) or cellular convection (Agee et al., 1973) has been recognized for decades. Meanwhile, the ubiquity of patterns in scattered shallow clouds (Bony, Semie, et al., 2020; Rasp et al., 2020; Stevens et al., 2020) and their relationship to mesoscale circulations in the atmosphere (George et al., 2023) has received stronger focus more recently. This is partly because it may be critical to understanding precipitation (Radtke et al., 2022) and the radiative budget (Bony, Schulz, et al., 2020).

In this study, we aim to investigate how low-level cloudiness, including its organization and accompanying mesoscale circulations, depend on parameterized (sub-grid) transport of heat, moisture, and momentum by shallow convection. We use a mesoscale or storm-resolving model with a horizontal grid spacing of 2.5 km on a domain of  $200 \times 200\text{ km}$  to answer: How does shallow convective transport influence trade-wind cloudiness and mesoscale circulations in simulations where shallow convection is either fully parameterized or (partially) resolved? Our study uses the High Resolution Local Area Modeling - Aire Limitee Adaptation dynamique Developpement InterNational (HIRLAM-ALADIN) Research on Mesoscale Operational NWP In Europe - Applications of Research to Operations at Mesoscale (HARMONIE-AROME) model. With this model we focus on the model intercomparison project (MIP) associated with EUREC4A (Stevens et al., 2021), an observational campaign that focused on trade-wind convection east of Barbados, following seminal field studies of this cloud regime (Holland & Rasmusson, 1973; Rauber et al., 2007).

Some of the goals of the EUREC4A-MIP are to assess the simulation capability of the observed shallow cloud mesoscale organization over the subtropical ocean, and understand the underlying dynamical processes leading to mesoscale organisational patterns. Our study specifically focuses on characterizing and explaining the differences between three model setups: (a) an experiment with fully parameterized transport of heat, moisture and momentum by shallow convection (control), (b) an experiment without parameterized momentum transport by shallow convection, and (c) an experiment without any transport by parameterized shallow convection (turning off the SCP altogether).

Our paper is organized as follows: Section 2 introduces the HARMONIE-AROME model and explains the parameterization of shallow convection in it. Section 3 introduces the experimental design with a description of the different model experiments (Section 3.1), the observational data (Section 3.2), and the tools used for the analysis (Section 3.3). We then compare modeled and observed time series (Section 4.1) and mean profiles (Section 4.2) of key atmospheric quantities, before analyzing the impact of the SCP on cloud statistics (Section 5),

on parameterized and resolved fluxes (Section 6), and on circulations (Section 7). In Section 8 we discuss the relation between changes in cloudiness and circulation. The conclusions are given in Section 9.

## 2. HARMONIE-AROME

Bengtsson et al. (2017) provide a general description of the numerical weather prediction model HARMONIE-AROME (HARMONIE hereafter) version cy40. Here we use the more recent version cy43. The relevant modifications in the physics in cy43 compared to cy40 are presented by de Rooy et al. (2022), together with a comprehensive description of the statistical cloud scheme, the (bulk) mass-flux convection scheme, and the turbulent kinetic energy (TKE) turbulence scheme (or eddy diffusivity scheme). HARMONIE uses the eddy-diffusivity mass-flux (EDMF) framework which facilitates a unified description of the turbulent transport in the dry convective boundary layer (Siebesma et al., 2007) and the cloud-topped boundary (Rio & Hourdin, 2008; Soares et al., 2004). This is a widely applied framework, which has often been extended for a unified representation of sub-grid scale turbulence and convection. For example, Tan et al. (2018) propose an extended EDMF scheme with explicit time-dependence and memory of sub-grid-scale variables, while Suselj et al. (2019a, 2019b) propose a multiplume EDMF where all plumes are initialized at the surface. Here we shortly review the formulation of parameterized transport and clouds in HARMONIE.

### 2.1. Parameterized Transport

The momentum budget for the zonal wind component  $u$  can be written as:

$$\frac{\partial \bar{u}}{\partial t} = -\bar{\mathbf{u}} \cdot \nabla \bar{u} - \frac{1}{\rho} \frac{\partial \bar{p}}{\partial x} + f\bar{v} - \frac{1}{\rho} \frac{\partial (\overline{w'u'})_{\text{subg}}}{\partial z}, \quad (1)$$

where the overline represents a grid box mean,  $\mathbf{u}$  is the wind vector,  $p$  is the atmospheric pressure,  $\rho$  the air density,  $f$  the Coriolis parameter,  $v$  is the meridional wind component, and  $(\overline{w'u'})_{\text{subg}}$  is the sub-grid zonal momentum flux. The sub-grid flux is divided into that carried by shallow convection (SC) and by turbulent transport modeled by the eddy diffusivity (ED) scheme:

$$(\overline{w'u'})_{\text{subg}} = \overline{w'u'}^{\text{SC}} + \overline{w'u'}^{\text{ED}}. \quad (2)$$

The first term on the rhs represents the non-local flux carried by the largest coherent (dry and moist) turbulent eddies, while the second term on the rhs represents the flux carried by the smaller scale turbulent eddies. A similar separation is applied for fluxes of liquid potential temperature  $\theta_l$  (heat), total specific humidity  $q_l$  (moisture), and meridional wind  $v$  (meridional momentum).

The SC parameterization in HARMONIE (de Rooy et al., 2022), hereafter referred to as the SCP, applies a dual updraft mass-flux (MF) approach (Neggers, 2009) and can be written as:

$$\rho \overline{w'\phi'}^{\text{SC}} \approx M_{\text{dry}} (\phi_{\text{u,dry}} - \bar{\phi}) + M_{\text{moist}} (\phi_{\text{u,moist}} - \bar{\phi}), \quad (3)$$

where  $\phi = [\theta_l, q_l, u, v]$  is a generic variable,  $M_{\text{dry}}$  and  $M_{\text{moist}}$  are the convective mass fluxes of the dry and moist updraft respectively. The updraft profiles  $\phi_{\text{u},i}$  ( $i \in [\text{dry, moist}]$ ) are determined by an entraining plume model.

The fractional entrainment of the dry updraft and the moist updraft in the sub-cloud are built on the formulation of Siebesma et al. (2007). These formulations depend on height ( $z$ ) and the inversion height. The fractional entrainment formulation of the moist updraft in the cloud layer is connected to the formulation of the moist updraft in the sub-cloud layer and decreases proportionally to  $z^{-1}$ . Finally, the detrainment in the cloud layer is formulated according to de Rooy and Siebesma (2008). Both entrainment and detrainment formulations are described in detail in de Rooy et al. (2022) and are supported by numerous LES studies (Boing et al., 2012; de Rooy et al., 2013; Jonker et al., 2006).

The SC scheme distinguishes between two different convective boundary layer regimes: dry convective boundary layers, with only a dry updraft, and cloud-topped boundary layers, with a dry and a moist updraft. In the formulation of the mass-flux approach, the treatment of momentum differs from that of scalar variables only in the initialization of the updraft properties at the lowest model level, whereby temperature and humidity are given a small excess value compared to the environment that is scaled by the surface fluxes, while  $u$  and  $v$  do not.

The small-scale turbulence parameterization can be written as:

$$\overline{w'\phi}^{\text{ED}} \approx -K \frac{\partial \bar{\phi}}{\partial z}, \quad (4)$$

where  $K$  is the eddy diffusivity. This is the ED component of the EDMF framework.

In this study we always consider both the dry- and moist-mass flux components together. In the experiments without the SCP, we omit all mass-flux contributions (dry + moist) and leave only the ED scheme active as a sub-grid transport process (see Section 3.1 for a description of the different experiments).

## 2.2. Parameterized Clouds and Precipitation

Low clouds are parameterized with a statistical cloud scheme (Bougeault, 1981; Sommeria & Deardorff, 1977). In such an approach, cloud cover and liquid water content are derived from estimates of the sub-grid variance of  $q_t$  and  $\theta_t$ . In the literature, several approaches exist to estimate these sub-grid variance (Bechtold et al., 1995; Golaz et al., 2002). De Rooy et al. (2022) describe the statistical cloud scheme as applied in HARMONIE. Both the ED and SC fluxes contribute to the sub-grid variance but in HARMONIE we apply an additional term with the characteristics of a relative humidity scheme (de Rooy & Siebesma, 2010). This means that, in the absence of convection and no noticeable amount of turbulent activity, the variance is still different from zero. The role of this extra variance term is to account for the effect of surface heterogeneity, horizontal large-scale advection, mesoscale circulations, and gravity waves.

Precipitation above the surface is determined by the microphysics within the grid box, while at the surface there can be a sub-grid contribution from the SC scheme. The sub-grid precipitation calculated in the updraft of the SC scheme is added only to the surface precipitation and not transferred to the grid box at the corresponding model level. This means that the sub-grid precipitation from the SC scheme cannot help in the development of mesoscale circulations (e.g., by evaporation). Turning off the SCP effectively removes a (small) source of surface precipitation and a source of sub-grid variance for  $q_t$  and  $\theta_t$ . The latter leads the cloud scheme to more easily produce fully cloudy or cloud free grid boxes, with less intermediate states.

## 3. The Setting

### 3.1. Experiments

We use HARMONIE to simulate an area of  $3,200 \times 2,025 \text{ km}^2$  over the North Atlantic trade-wind region with a horizontal grid spacing of 2.5 km. The analysis domain spans  $200 \times 200 \text{ km}^2$  centered at 13.28 N and 57.76 W, a key region in EUREC4A studies (Savazzi et al., 2022, 2024). HARMONIE receives lateral boundary fields from ERA5 (Hersbach et al., 2020) every hour and the SST is updated every 24 hr. The runs are performed in a free (climate) mode for 2 months, from 1 January to 29 February 2020. In climate mode, HARMONIE is initialized only once at 1 January, which limits the effects of biases inherited from the forcing model. With this setup there are no discontinuities in the time series. The model can more freely develop its dynamics in response to varying large-scale forcing.

The 2 months of simulation allow us to address the response of clouds and convection across a wide range of conditions and different mesoscale organisation, during a period for which extensive observations are available. The model physics respond very quickly to changes in dynamical forcing, and that forcing generally changes substantially on sub-daily and intra-daily time scales, such that differences do not build up over time. As our results in Section 4.1 will show, the response of cloudiness to parameterized convection can be very different from day-to-day, depending on the large-scale forcing that may make the environment more conducive to (explicitly) resolving convection.

We perform three experiments with different representation of  $\overline{w'\phi}^{\text{SC}}$  under convective conditions.

1. A control run with the operational setup as used in (Savazzi et al., 2024):

$$\text{Control : } \overline{w'\phi}^{\text{SC}} \neq 0 \quad \text{with } \phi = [\theta_l, q_l, u, v], \quad (5)$$

where both the SC (dry + moist MF) and the ED scheme are active.

2. A run without SCP (dry + moist MF) for horizontal momentum, whereby the SCP remains active for heat and moisture:

$$\begin{aligned} \text{UV-OFF : } \overline{w'\phi}^{\text{SC}} &\neq 0 \quad \text{with } \phi = [\theta_l, q_l], \\ \overline{w'u}^{\text{SC}} &= 0 \quad \overline{w'v}^{\text{SC}} = 0. \end{aligned} \quad (6)$$

3. A run where the SCP (dry + moist MF) is turned off completely:

$$\text{SC-OFF : } \overline{w'\phi}^{\text{SC}} = 0 \quad \text{with } \phi = [\theta_l, q_l, u, v] \quad (7)$$

The ED scheme and the cloud scheme remain active in all simulations; thus the model can respond to the removal of mass-flux transport by adjusting both the resolved and sub-grid ED transport.

### 3.2. Observations

We use the following observations to evaluate the realism of the model experiments.

1. Images from GOES16 (NOAA, 2020), the first of the Geostationary Operational Environmental Satellite R (GOES-R) series. Spaceborne instruments have proven useful in assessing cloud patterns in the trades (Bony, Schulz, et al., 2020; Schulz, 2022), despite challenges in detecting shallow cumuli because of their small footprint and low optical depth, and overlying mid- and high-level clouds (Marchand et al., 2010; Zhao & Di Girolamo, 2006). From GOES16, we use channel 13 of the Advanced Baseline Imager (ABI), which provides brightness temperature at a spatial resolution of 2 km. We extract 1,140 images of the analysis domain with a temporal resolution of 1 hr, which are regridded to 2.5 km to match the resolution of HARMONIE. We define a marine low-cloud mask using measurements with a brightness temperature between 270 and 292 K. Cloud top height (CTH) is derived assuming a constant dry adiabatic lapse rate of 10 K km<sup>-1</sup> up to 700 m and a moist adiabatic lapse rate of 6.5 K km<sup>-1</sup> aloft. These numbers allow us to include somewhat deeper clouds than in Bony, Schulz, et al. (2020), which used 280 and 290 K as thresholds.
2. Radiosondes from the Barbados Cloud Observatory (BCO) (Stephan et al., 2021). More than 300 radiosondes were launched at 13.1 N and 59.3 W during EUREC4A, between 16 January and 17 February. The interval between consecutive launches varies between two and three hours.
3. The JOANNE (Joint dropsonde Observations of the Atmosphere in tropical North atlaNtic mesoscale Environments) data set (George et al., 2021). We use Level 3 of this data set, which comprises around 1,000 dropsondes launched from the high-altitude and long-range research aircraft HALO during EUREC4A, between 19 January and 15 February, along a ~220 km diameter circle centered at 13.3 N, 57.7 W.

### 3.3. Tools

The cloud fields are analyzed using organization metrics define by Janssens et al. (2021). For GOES16 the cloud mask is defined in Section 3.2; while for HARMONIE, any grid box in the lower 4 km with a cloud fraction larger than 0.5 is considered cloudy. A number of organization metrics require further explanation.

1. Cloud size is determined by the square root of its area, projected onto the surface. In other words, cloud size is the length of one side of a square that has the same area as the cloud object.
2. Cloud cover (CC) is the fractional area covered by clouds projected onto the surface plane. In this study we consider cloudy grid cells only up to 4 km.



3. Open sky is the fraction covered by the largest possible rectangle placed in the domain without touching any cloud, and is thus a measure of the cloud-free area.
4. Orientation is a dimensionless quantity between 0 and 1, with 0 denoting that clouds have no preferential direction of orientation and 1 denoting that all clouds are oriented in one direction.

We also apply the organization metrics to the flow field. We identify shallow mesoscale overturning circulations (SMOCs) as in George et al. (2023). These are regions where the sub-cloud (0–600 m) and the cloud layers (900–1,500 m) exhibit mesoscale horizontal divergence  $D$  with the opposite sign. The sign of the divergence in the sub-cloud layer ( $D_{sc} = \frac{\partial u}{\partial x} + \frac{\partial v}{\partial y}$ ) reveals mesoscale ascent ( $D_{sc} < 0$ ) or mesoscale subsidence ( $D_{sc} > 0$ ).

After smoothing the fields of  $D$  to 20 km (see Savazzi et al. (2024) for the filtering method) we only consider grid boxes where  $|D|$  is greater than  $\pm 10^{-6} s^{-1}$ . This is a fairly small threshold compared to the values of the  $D$  dipole ( $D'$ ) found in the domain (shown later in Section 7). We define the following metrics.

1. The  $D$  dipole ( $D'$ ) strength (or SMOC strength) is the difference between the cloud layer and the sub-cloud layer divergence ( $D' = D_c - D_{sc}$ ).
2. SMOC coverage, similar to CC, is the fractional area covered by SMOCs.
3. Aspect ratio is the non-dimensional ratio between (horizontal) SMOC size and its vertical extent, where the size is defined as for the cloud objects, while the vertical extent is the height of maximum divergence when  $D_{sc} < 0$  and minimum divergence when  $D_{sc} > 0$ .

In our analysis of the mesoscale circulations we also apply Reynolds decomposition and identify fluctuations  $\phi'_{res}$  of a generic variable  $\phi$  at the 2.5 km grid resolution with respect to the slab average  $\langle \phi \rangle$  taken over the  $200 \times 200$  km<sup>2</sup> analysis domain. This allows to distinguish between parameterized sub-grid fluxes  $(\phi'w')_{sbg}$  and resolved fluxes  $(\phi'w')_{res}$ . The total turbulent flux in the domain is thus defined as:

$$(\phi'w')_{total} = (\phi'w')_{sbg} + (\phi'w')_{res} \quad (8)$$

We drop the subscript for the variances of the fluctuations  $\phi'_{res}$  at scales larger than 2.5 km, thus  $\overline{\phi'^2_{res}} = \sigma_{\phi}^2$ .

Wind variances at scales larger than 2.5 km ( $\sigma_u^2, \sigma_v^2, \sigma_w^2$ ) can be combined to define the eddy kinetic energy (EKE), as a proxy of mesoscale variability and intensity of resolved eddies:

$$EKE = \frac{1}{2}(\sigma_u^2 + \sigma_v^2 + \sigma_w^2). \quad (9)$$

Following Salesky et al. (2017) we also define the EKE anisotropy as the ratio  $\sigma_w^2/(\sigma_u^2 + \sigma_v^2)$ , which helps indicate the relative importance of buoyancy and shear production of vertical and horizontal wind variance.

## 4. Characteristics of the Simulated Period

### 4.1. Time Series

The temporal variability in cloudiness driven by different mesoscale and synoptic conditions is rich in the trades (Nuijens et al., 2014; Vogel et al., 2022). Compared to dropsonde measurements (the JOANNE data set collected during EUREC4A), all three HARMONIE experiments reasonably capture the evolution of the wind speed in the lower 200 m, plotted as a 24-hr rolling average in Figure 1d. While the left panel of Figure 1 shows the temporal evolution of selected quantities, the box charts in the right panel show their distribution over the 2 months. The triangles indicate the mean, the boxes indicate the interquartile range, and the whiskers indicate the extremes.

Satellite observations from GOES16 (orange in panel e) show that the domain mean cloud top height is also in the right ballpark, although with more pronounced variability in the model. In the first half of January and first half of February, the modeled clouds deepen more than what observed. When the winds weaken in the second half of January the modeled cloud field oscillates between deeper clouds with large CC (panel f), and shallower cloud tops with low CC, while GOES16 shows a more constant mean CTH of about 1.5 km.

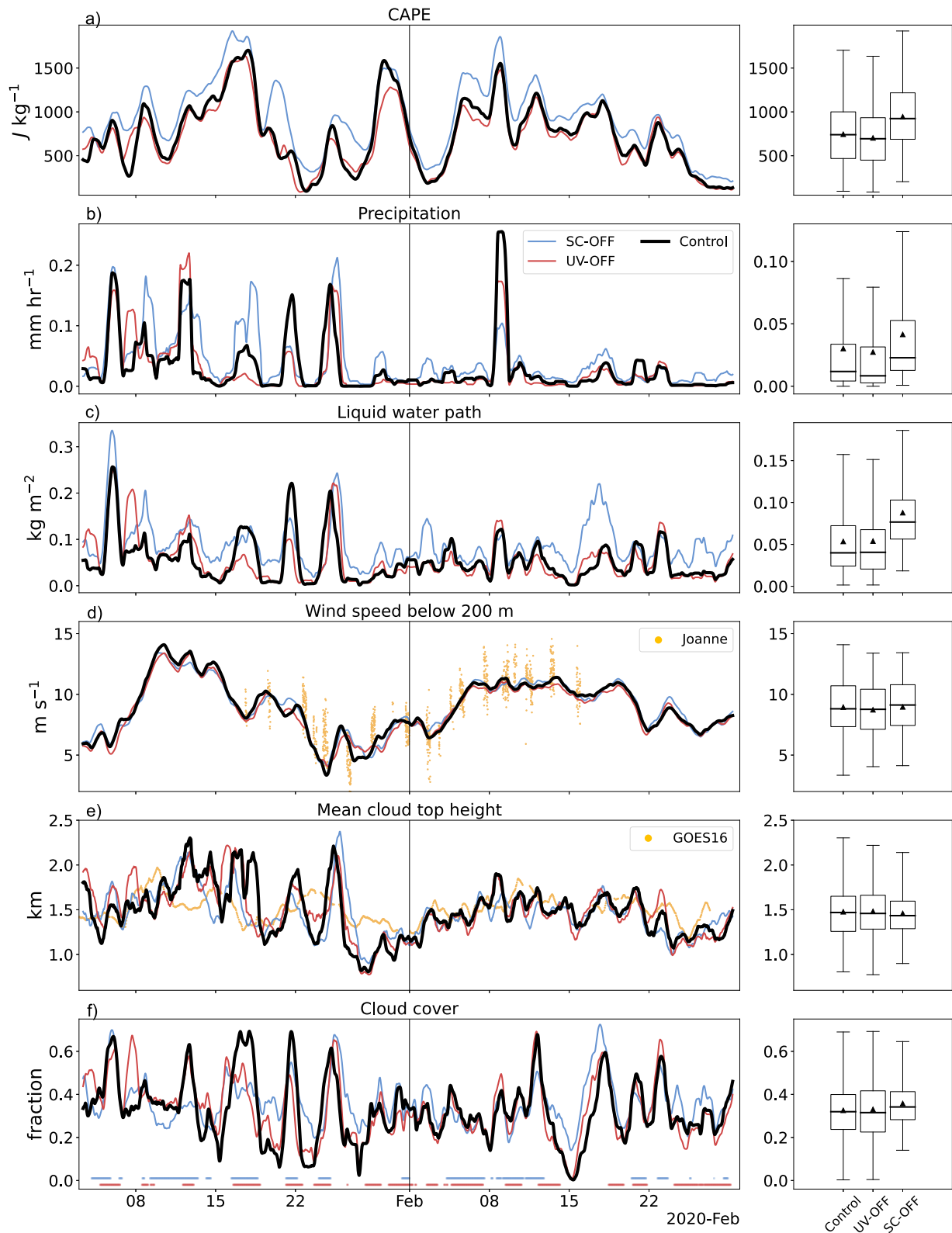


**Figure 1.** Temporal evolution (left column) and distribution (right column) of (a) convective available potential temperature CAPE, (b) surface precipitation, (c) liquid water path LWP, (d) mean wind speed of the lower 200 m, (e) mean cloud top height CTH, (f) cloud cover CC below 4 km. The time series are shown as 24-hr rolling averages. The dots at the bottom of panel (f) mark times where  $CC_{UV-OFF} < CC_{control}$  (red), and  $CC_{SC-OFF} < CC_{control}$  (blue). Black is for the control, red for UV-OFF, and blue for SC-OFF. The orange dots indicate dropsonde measurements from JOANNE in panel (d) and satellite measurements from GOES16 in panel (e).



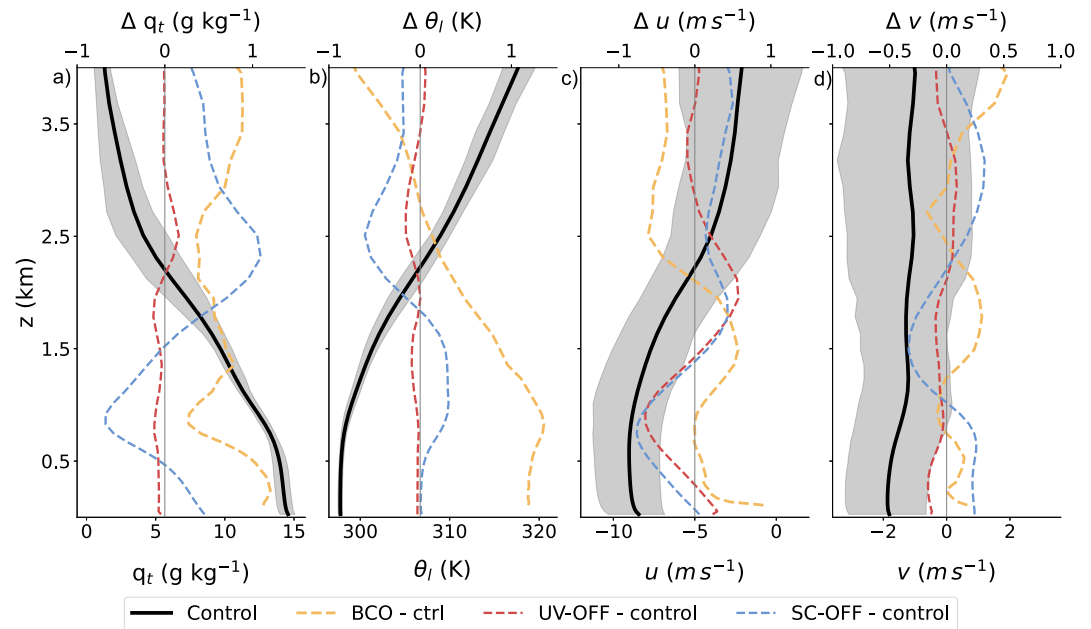


**Figure 2.** Mean profiles of (a) specific humidity  $q_t$ , (b) liquid potential temperature  $\theta_l$ , (c) zonal  $u$ , and (d) meridional  $u$  wind. The bottom  $x$ -axes display the mean (solid black) and interquartile range (shading) of the control experiment. The top  $x$ -axes display the mean difference of the observations and other experiments to the control: observations (BCO) - control (orange), UV-OFF - control (red), SC-OFF - control (blue).

The mean CC is surprisingly similar among the three experiments, as seen in the box chart of panel (f), although the distribution narrows for the SC-OFF experiment. However, on a daily basis, differences in CC between the experiments as large as 20% are not unusual, and they are both positive and negative, explaining why differences are small in the mean. In the time series, we use colored dots at the bottom of panel (f) to highlight hours where CC in SC-OFF is smaller than the control (blue dots), and where CC in UV-OFF is smaller than the control (red dots). About 40% of the time,  $CC_{SC-OFF} < CC_{control}$ , whereas  $CC_{UV-OFF} < CC_{control}$  about 49% of the time. We will make use of this distinction later in Section 5 when we describe how this relates to changes in cloud organisation and wind speed.

The evolution of mean CTH and CC in HARMONIE is not strictly tied to the convective available potential energy (CAPE), which is shown in Figure 1a. For example, the peak in CAPE captured by all experiments at the end of January is not associated with any rapid increase in mean CTH nor in CC. Nevertheless, CAPE in SC-OFF is about  $250 \text{ J kg}^{-1}$  higher on average, suggesting that the absence of SC helps build up instability that would otherwise be quickly removed. Panels (b) and (c) further indicate more mean precipitation and higher liquid water path (LWP) in SC-OFF.

#### 4.2. Mean Profiles

The mean thermodynamic and dynamic profiles of the control experiment, along with the interquartile range to indicate the variability, are shown in Figure 2 as black lines and shaded areas. The profiles of specific humidity  $q_t$  (panel a) and liquid potential temperature  $\theta_l$  (panel b) show a relatively well-mixed boundary layer reaching 600 m, with a weak trade-inversion in  $\theta_l$  between 2 and 2.5 km. The warm, moist surface layer and a strong easterly breeze ( $\sim 10 \text{ m s}^{-1}$  in panel (c)) establish the typical environment of trade-wind shallow cumulus convection (Nuijens et al., 2014). Near cloud base, between 700 and 800 m, the zonal wind  $u$  has a local maximum, or low-level wind jet (Larson et al., 2019). The meridional wind is weaker than the zonal wind, with values around  $-2 \pm 1 \text{ m s}^{-1}$  below 600 m, and  $-1 \pm 1 \text{ m s}^{-1}$  above.

Figure 2 also shows the mean differences of UV-OFF (red), SC-OFF (blue), and the BCO soundings (orange) with respect to the control. The dashed orange line in panel (a) and (b) shows that the control is about  $1 \text{ g kg}^{-1}$  too dry in the lower 500 m and 1 K too cold in the lower 1 km compared to the BCO soundings, a bias that is inherited from ERA5 (not shown). In SC-OFF, the profile of  $q_t$  improves with respect to the observations in the lower few hundred meters and above 1.5 km, because the difference between SC-OFF and the control (dashed blue) has the same sign as the difference between the BCO soundings and the control. Still, SC-OFF is too dry around cloud base and too moist at cloud top (2.5 km).

In SC-OFF, the profiles of  $q_t$  and  $\theta_t$  are better vertically mixed in the cloud layer: drier and warmer than the control around 1 km, and moister and colder than the control at 2.5 km. This suggests that non-local transport of heat and moisture from the lower to the upper cloud layer is more efficient when done by resolved eddies in SC-OFF than by the parameterization in the control. In contrast, without SCP the sub-cloud layer humidity becomes less well-mixed, highlighting the importance of the sub-grid transport by dry MF. The removal of parameterized momentum transport by SC (UV-OFF) has a negligible effect on the mean thermodynamic profiles. From Figure 2a, the main difference between UV-OFF and the control run is a somewhat moister layer near 2.5 km in UV-OFF (dashed red line), which relates to enhanced cloudiness at this level, which we return to below.

In terms of the horizontal wind profiles (Figures 2c and 2d), SC-OFF and UV-OFF have more wind shear on average than the control. Momentum transport by the SCP acts to mix winds across the boundary layer for example, by transporting zonal momentum from the surface upwards into the cloud layer. The result is less shear throughout the lower troposphere when the SCP is active, with reduced zonal wind jet at 700 m and stronger winds between 1.5 and 2.5 km. A comparison between the orange line and the blue and red lines in panel (c) reveals that the zonal wind jet that develops without parameterized momentum transport by SC is too strong and the wind shear becomes too large compared to the observations. Sandu et al. (2020) showed a similar effect of parameterized shallow convective mixing for the ECMWF-IFS (ECMWF, 2024) at 40 km resolution. They observed that the zonal wind jet developing without momentum transport by SCP in the ECMWF-IFS is too strong compared to observations and reanalysis, although the lack of mixing reduces the surface bias (Savazzi et al., 2022).

The largest effect on the zonal wind comes from the removal of parameterized momentum transport by the SCP. Further removing the parameterized transport of heat and moisture in SC-OFF does not significantly change the zonal wind. This is not the case for the meridional wind, which weakens in SC-OFF, producing a veering of the wind and a weaker meridional component, while the surface winds in UV-OFF turn southward, acquiring a stronger meridional component. These differences in the mean winds do not directly translate into different mesoscale circulations (which we describe in Section 7), but help understand how parameterized shallow convection modulates the large scale flow feeding into the ITCZ. Overall, we find that HARMONIE reproduces observed zonal and meridional wind profiles better in the control, which highlights that sub-grid momentum transport by SC is non-negligible.

In SC-OFF the model produces more resolved convection as a way to compensate for the missing parameterized SC fluxes, while in UV-OFF the resolved fluxes remain similar to the control. We will return to the flux transport and its partition between resolved and parameterized, in Section 6.1. Here we first analyze the differences in convective activity through profiles of vertical velocity. Figure 3a shows the mean and interquartile range for the variable  $w^{UP}$  as a proxy for resolved updraft strength. We define  $w^{UP}$  as the positive resolved vertical velocity  $w$  sampled in columns with at least one cloudy grid box at any level. In SC-OFF,  $w^{UP}$  is twice that of the control (and of UV-OFF) throughout the cloud layer, with mean values of  $\sim 0.12 \text{ m s}^{-1}$  at 1 km.

Stronger resolved vertical velocity drives deeper clouds as shown by the normalized probability density function (PDF) of CTH in Figure 3b. For all data sets, this distribution peaks just above cloud base, at  $\sim 800 \text{ m}$ , and below the inversion, at  $\sim 2 \text{ km}$ . Deeper clouds in SC-OFF are associated with a higher probability of finding clouds above 2 km. Below the trade-inversion, here near 2 km, stratiform outflow layers, very similar to anvils found near the tops of deep cumulus, are common (Nuijens et al., 2014). SC-OFF produces less of these layers here, in line with previous studies that have found that the deepening of the cloud layer leads to reduced inversion strength and less stratiform cloudiness (Vogel et al., 2020).

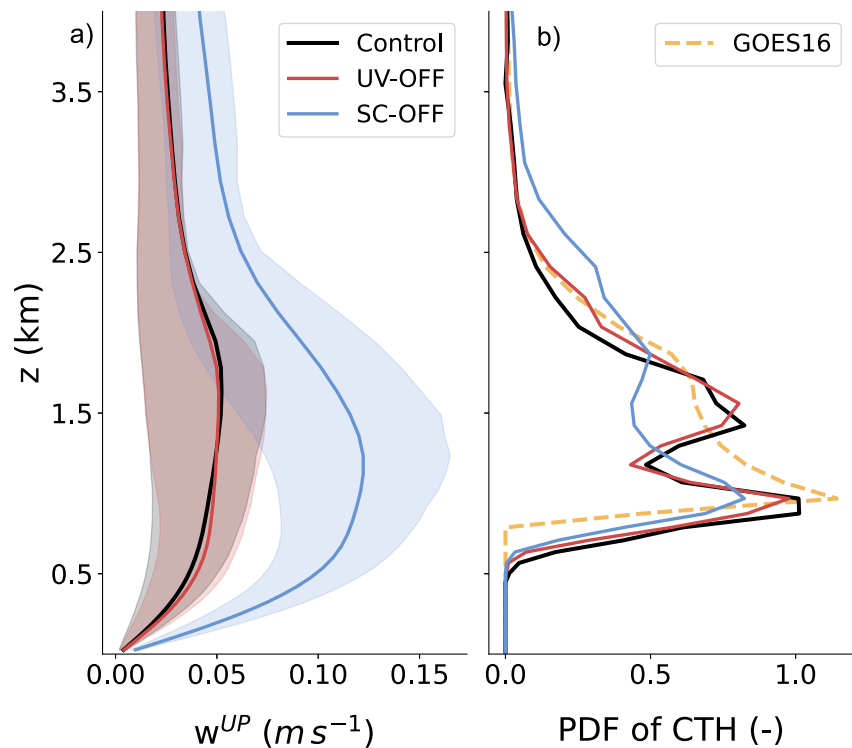


**Figure 3.** Profiles of (a) resolved updraft  $w^{UP}$ , and (b) normalized histogram (or PDF) of cloud top height CTH averaged over 2 months.  $w^{UP}$  is the positive resolved vertical velocity  $w$  when there is a cloud somewhere in the column. In (a) the solid lines indicate the mean, while the shadings indicate the interquartile range. Black is for the control, red for UV-OFF, blue for SC-OFF, and orange for the observations (GOES16).

Without parameterized momentum transport by SC (UV-OFF),  $w^{UP}$  does not change markedly (panel a), and neither does the overall distribution of CTH. However, as we will show in the next section, UV-OFF does on many days have a tendency to produce enhanced stratiform cloudiness and larger mean cloud sizes.

## 5. Cloud Statistics

In the simulated period various cloud patterns were simulated in HARMONIE. Quantifying these is important to validate the model's performance across the gray-zone. Figures 4a and 4b show two snapshots of CTH from GOES16. On 13 January at 12:00 LT (a) the cloud field is relatively unorganized with small clouds scattered throughout the domain, while on 13 February at 12:00 LT (b) the cloud field is highly organized with two large objects elongated in the south-west to north-east direction. Figure 4c quantifies the organisation of the cloud fields through orientation (y-axis) and open sky (x-axis), which have been introduced in Section 3.3. 13 January at 12:00 LT and 13 February at 12:00 LT are marked in the phase space with green crosses, which show that the clouds in panel (b) have a stronger preferential orientation than clouds in panel (a), and they allow for a larger cloud free area between object. All other images from GOES16 are represented by the orange dots and suggest that the relationship between orientation and open sky is not linear. Nevertheless, when clouds are aligned in a preferential direction (high orientation) there are larger patches of clear sky (high open sky).

In Figure 4c we compare the statistical distribution of orientation and open sky for the HARMONIE experiments, where the control is in black, UV-OFF is in red, and SC-OFF is in blue. For these, we use probability density functions (univariate in the external panels) and box charts (bivariate in the phase space), instead of scatter-plots. For each data set the box charts intersect at the mean. SC-OFF tends to have cloud fields similar to panel (a), while the control and UV-OFF show more frequent cloud fields similar to panel (b), with distributions of orientation and open sky comparable to GOES16 (orange).

This purely geometrical evaluation shows that SC-OFF produces different organisation patterns than the observation and other experiments. Smaller values of open sky, with relatively similar cloud cover (see

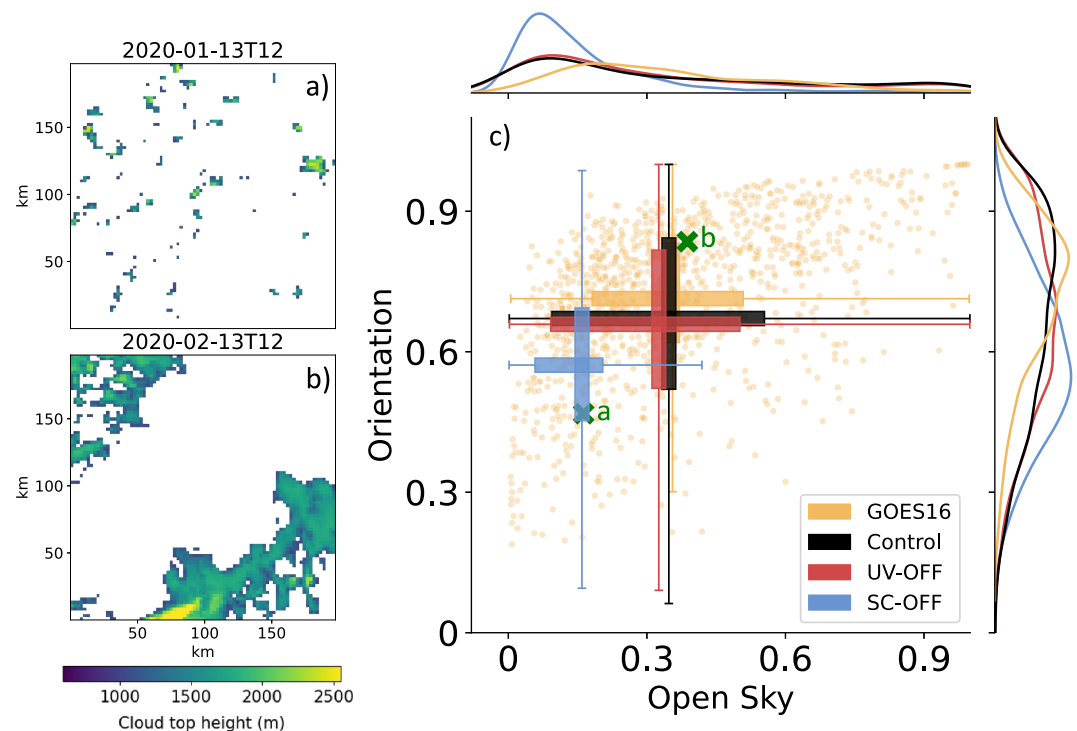


**Figure 4.** Snapshots of cloud top height (CTH) from GOES16 on (a) 13 January at 12:00 LT, and (b) 13 February at 12:00. In panel (c) is the phase space for the cloud metrics orientation (y-axis) and open sky (x-axis), where the instances in (a) and (b) are marked with green crosses. The orange dots refer to all other GOES16 images. The distributions are shown also as probability density functions (lines) and box charts for GOES16 (orange), the control (black), UV-OFF (red), and SC-OFF (blue). For each data set the box charts indicate interquartile range and extremes, and they cross at the mean.

Section 4.1), indicate a more "spotty" cloud field, where clouds are smaller and more homogeneously distributed. Images from GOES16, the control, and UV-OFF instead reveal a wider distribution of open sky with a mean around 0.4. For GOES16, the lower tail of the distribution is shifted to larger values, because small clouds are difficult to see from space. The orientation of projected clouds is less preferential in SC-OFF, with a mean orientation  $< 0.6$ , compared to  $\sim 0.7$  from GOES16. This indicates clouds that are too symmetric (round) in SC-OFF, which may be a result of stronger updrafts reaching higher, rather than becoming negatively buoyant near the inversion and producing spreading stratiform outflow.

The difference in convective activity modulates cloudiness in a non-trivial way. Cloud cover, can be split into a contribution from grid columns with clouds below 1 km and a residual contribution from grid columns that are cloudy above 1 km, without any cloud underneath. Stratiform cloud anvils are an important contributor to the latter (Nuijens et al., 2014). In Figure 5, this partition shows important differences among the three experiments, which are not evident from the total CC in Figure 1f.

Compared to the control, SC-OFF shows increased CC near cloud base, from 0.1 to 0.15. Above 1 km, the mean contribution remains similar to the control, but the distribution indicates a smaller maximum, suggesting that SC-OFF produces less stratiform outflow than the control. Clouds respond in the opposite manner in UV-OFF, with marginally smaller CC near cloud base, but more CC aloft, indicating more frequent stratiform outflow.

In Figure 6 we use total CC (below and above 1 km) to divide the time series into subsets of hours in which responses can be very different than the mean. Each experiment is compared to the control for those subsets during which CC is larger than the control (solid) or smaller than the control (dashed). Cloud cover (e), (f) combines information on the number of clouds (a), (b) and their size (c), (d) (defined in Section 3.3).

Clouds are equally numerous in UV-OFF and in the control (a). The mean size of the projected clouds, which is strongly influenced by the presence of stratiform outflows, determines the differences in CC between UV-OFF

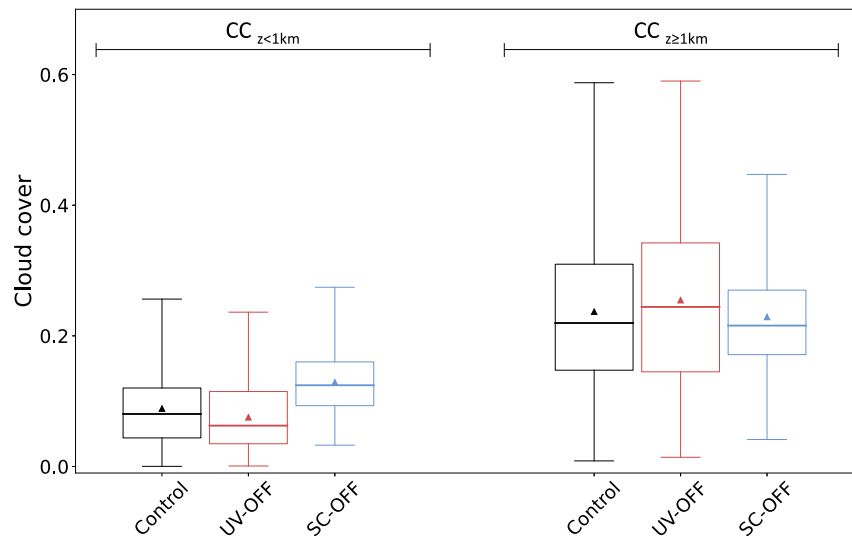


**Figure 5.** Contribution to total cloud cover from layers below (left side) and above (right side) 1 km. Black is for the control, red for UV-OFF, and blue for SC-OFF. Box limits indicate the range of the central 50% of the data (interquartile), with a central line marking the median. The triangle indicates the mean, and the whiskers capture the range of the remaining data.

and the control: larger clouds increase CC, while smaller clouds decrease CC. This translates to a clear negative correlation between CC (e) and open sky (g), meaning that open sky reduces as clouds become larger.

This relationship between CC and open sky changes in SC-OFF. In SC-OFF the distribution of all cloud metrics is narrower compared to UV-OFF and the control, except for CTH. Clouds are always more numerous in SC-OFF, but they are smaller. SC-OFF produces fewer stratiform outflows, and the larger number of clouds in SC-OFF is not always enough to compensate, so that CC decreases. Comparing the solid blue and black box charts draws the picture that more clouds in SC-OFF, despite being smaller, help make larger cloud cover, except when the control experiment makes stratiform anvils, as evident from the increase in mean cloud size (dashed black in panel d).

Figures 6i and 6l reveal changes in the depth of convection by means of CTH. The CTH statistics are very similar for UV-OFF and the control (panel i), while SC-OFF (panel l) has a wider distribution of CTHs, ranging from below 1 km to above 2.5 km, when  $CC_{SC-OFF} > CC_{control}$ , and even up to 3 km when  $CC_{SC-OFF} < CC_{control}$ . This highlights the connection between resolved updraft strength and total (low) cloud cover, as described in Vogel et al. (2020). When convection gets stronger, there is less detrainment below the inversion (at about 2 km), and less stratiform cloud, which has a large contribution to total cloud cover.

Space-borne observations over the western North Atlantic reveal that trade-wind clouds favor specific mesoscale patterns under specific environmental conditions (Bony, Schulz, et al., 2020). Isolated smaller cumulus clouds (*sugar*) are favored in more unstable boundary layers and weak winds. This environment promotes frequent updrafts, but weak winds and smaller surface fluxes generally make for a drier environment and raise the lifting condensation level. In these conditions, the SC-OFF experiment tends to produce more CC (near cloud base) than the control by promoting stronger updrafts, see Figure 6n.

Precipitating cumulus convection with cold pools (*gravel*) and with stratiform outflows (*flowers*) are favored in more stable boundary layers and strong winds. This environment promotes moistening of the boundary layer and larger cloud clusters, but a more stable lower troposphere prevents clouds from deepening, and detrainment promotes stratiform outflow. In these conditions, UV-OFF promotes larger changes in stratiform cloudiness (Figure 6m).

## 6. Impact on Fluxes and Variances

Without dry and moist MF contributions to transport, the eddy diffusivity (ED) scheme and the resolved dynamics will carry all the flux (Section 2.1). In SC-OFF, all fluxes (moisture, heat, and momentum) change in response to the missing MF, while in UV-OFF only the momentum fluxes need to adjust (although other indirect effects might

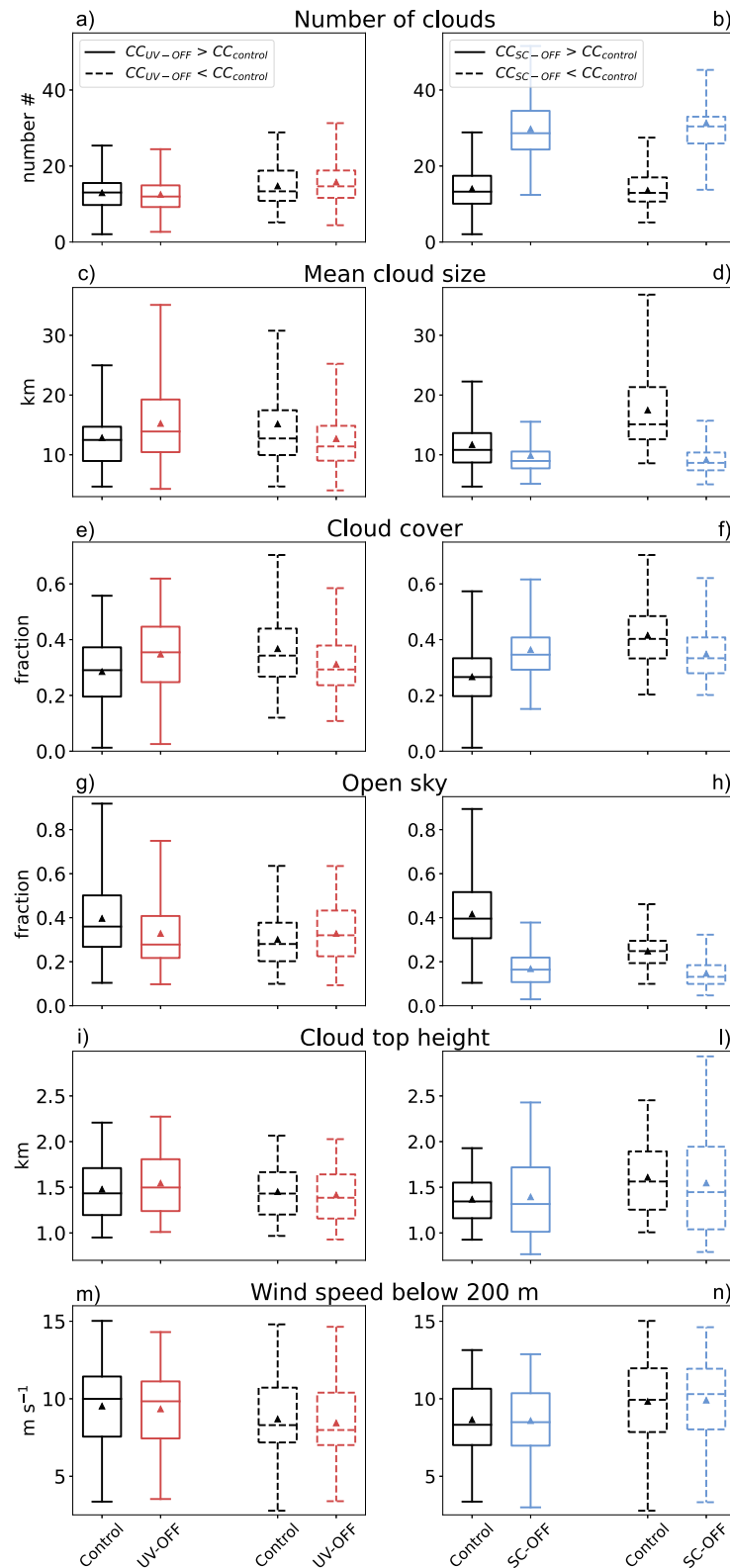


**Figure 6.** Distribution of key cloud metrics (a to l) and surface-layer wind speed (m, n) grouped by instances where  $CC_{UV-OFF} > CC_{control}$  (left panels, solid lines),  $CC_{UV-OFF} < CC_{control}$  (left panels, dashed lines),  $CC_{SC-OFF} > CC_{control}$  (right panels, solid lines), and  $CC_{SC-OFF} < CC_{control}$  (right panels, dashed lines).



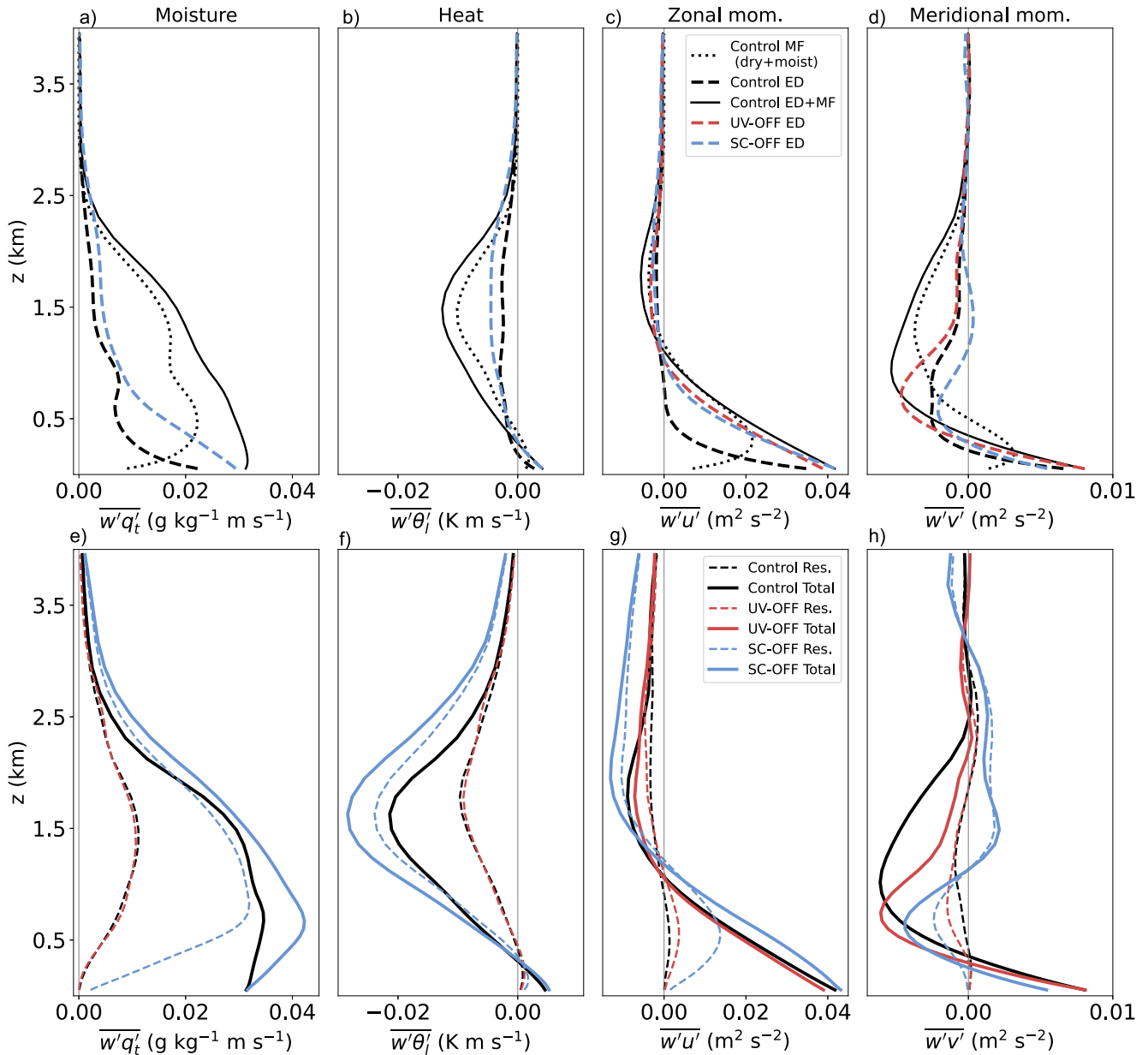


**Figure 7.** Mean in space and time of the flux profiles for moisture (a), (e), heat (b), (f), zonal momentum (c), (g), and meridional momentum (d), (h). On the top row (a), (b), (c), (d) the parameterized flux (solid) is divided into the SC scheme (dotted), which includes dry and moist MF, and the ED scheme (dashed). The SC scheme is turned on in the control (black), and turned off in SC-OFF (blue). On the bottom row (e), (f), (g), (h) is the resolved flux (dashed) and the total flux (solid), which is the sum of the parameterized and resolved fluxes.

cause secondary adjustments to the heat and moisture fluxes). In Figure 7 we investigate how HARMONIE partitions the total fluxes between parameterized and resolved fluxes, and how these change in the three experiments.

In the top row of Figures 7a–7d we show the parameterized fluxes  $(\overline{\phi'w'})_{\text{sbg}}$ , comprising the MF contribution (dotted lines, where active) and the ED contribution (dashed lines). Panels e, f, g, h on the bottom row display the resolved fluxes  $(\overline{\phi'w'})_{\text{res}}$  as dashed lines, and the total fluxes  $(\overline{\phi'w'})_{\text{total}}$  as solid lines. The sub-grid fluxes of moisture and heat from UV-OFF were not saved and thus not shown, but given the unchanged thermodynamic structure in UV-OFF compared to the control, we anticipate that these fluxes are very similar to the control.

The SCP (dotted black in panels a–d) introduces fluxes that are largest in the cloud layer and reduce to zero at the surface and at 2.5 km, above the cloud layer. The ED scheme (dashed in panels a–d) introduces fluxes that are largest near the surface. Focusing on the parameterized moisture flux (panel a), we see that the ED component increases across all heights when the SCP is turned off. At the surface this goes from  $0.02 \text{ g kg}^{-1} \text{ m s}^{-1}$  in the control to  $0.03 \text{ g kg}^{-1} \text{ m s}^{-1}$  in SC-OFF, compensating for the absence of the SCP, as the dashed blue line is closest to the combined ED and MF components in the control (solid black). At other levels below 2.5 km, however, the increase in ED flux is insufficient, with the combined ED and MF in the control being more than double the ED flux in SC-OFF (dashed blue).

The combined ED + MF zonal momentum flux (solid black in panel c) has a profile that can be represented well by the ED approach alone: large, positive near the surface and reducing to zero above cloud base, around 1 km. In this case, removing the parameterized momentum transport by SC causes the ED component to increase, producing a similar parameterized flux in SC-OFF and UV-OFF as in the control (solid black), but only in the sub-cloud layer. Compared to the control, the parameterized zonal as well as the meridional momentum flux in SC-OFF and UV-OFF is substantially weaker near cloud base and in the cloud layer up to 2 km, which helps explain the larger wind shear and stronger zonal wind jet that develops in these experiments (Figures 2c and 2d).

The resolved transport also adjusts, as shown by the dashed lines in Figures 7e–7h. This adjustment, combined with adjustments in MF and ED fluxes, set the heat, moisture and momentum tendencies and thus the mean profiles (see Figure 2). The resolved moisture flux (panel e) in SC-OFF increases from about  $0.01 \text{ g kg}^{-1} \text{ m s}^{-1}$  to  $0.03 \text{ g kg}^{-1} \text{ m s}^{-1}$  at 1 km compared to the control, and the resolved heat flux increases from about  $-0.01 \text{ km s}^{-1}$  to  $-0.03 \text{ km s}^{-1}$  at 1.5 km. The resolved momentum fluxes in UV-OFF (dashed red in bottom row) increase primarily in the cloud layer, but while this brings the total zonal momentum flux from UV-OFF (solid red in panel g) very close to the control (solid black), the total meridional momentum flux is less in UV-OFF compared to the control. This helps explain, as we show in the next section, that resolved momentum variance increases in UV-OFF in the presence of weaker sub-grid momentum fluxes.

In SC-OFF, the combination of increased ED and resolved fluxes produce a total flux (solid lines in panels e–h) that exceeds the fluxes of moisture, heat, and zonal momentum in the control. Notably, in this configuration, the resolved flux alone can surpass the total flux in the control. As we show next, the enhanced resolved heat and moisture transport can drive stronger mesoscale circulations, in line with Janssens et al. (2022).

### 6.1. Eddy Kinetic Energy

Spatial variability in the trade-winds is known to be rich from both observations (George et al., 2023; Vogel et al., 2022) and simulations (Savazzi et al., 2024). Presumably, a change in the total heat, moisture and momentum fluxes and in the character of clouds brings about a change in resolved circulations on mesoscales. With a 2.5 km grid spacing, resolved circulations are somewhat artificial, as individual updrafts and the effect of cold pools cannot be captured (Kurowski et al., 2024; Lamaakel & Matheou, 2022). Despite this constraint, we use the resolved eddy kinetic energy (EKE), defined in Section 3.3 to measure wind fluctuations ( $u'_{\text{res}}, v'_{\text{res}}, w'_{\text{res}}$ ) at scales larger than 2.5 km. This can indicate to what extent the flow field is gaining or losing energy in response to stronger convection in SC-OFF and less sub-grid momentum flux, at least in the cloud layer, in UV-OFF.

Figure 8a shows the mean profile and interquartile range of EKE for each experiment and reveals that EKE in the cloud layer increases in UV-OFF and further increases in the sub-cloud layer as well when SC becomes resolved in SC-OFF. Figure 8b shows EKE as a function of spatial scale, which is computed by progressively coarsening the wind field and computing the EKE for all mesh sizes between 2.5 and 200 km. The contribution of each scale is shown as a percentage to the total EKE at 1 km, just above cloud base. This contribution is largest at the smallest spatial scales, declining quickly beyond 2.5–50 km. The decline is largest for SC-OFF, in which 50% of the total resolved EKE is carried at scales less than 50 km, compared to 35% and 40% in the control and UV-OFF, respectively. Of the three experiments, UV-OFF has the largest contribution of scales between ~25 and 100 km, and more EKE in the cloud layer compared to the control.

In SC-OFF both shear and buoyancy production of EKE increase in the sub-cloud layer, as shown in Figures 9a–9c. The shear production terms are defined as  $-\frac{\partial \bar{u}}{\partial z}(\overline{w'u'})_{\text{res}}$  (a) and  $-\frac{\partial \bar{v}}{\partial z}(\overline{w'v'})_{\text{res}}$  (b), the buoyancy production term is defined as  $\frac{g}{\theta_v}(\overline{w'\theta'_v})_{\text{res}}$  (c). The buoyancy production term is overall two orders of magnitude smaller than the

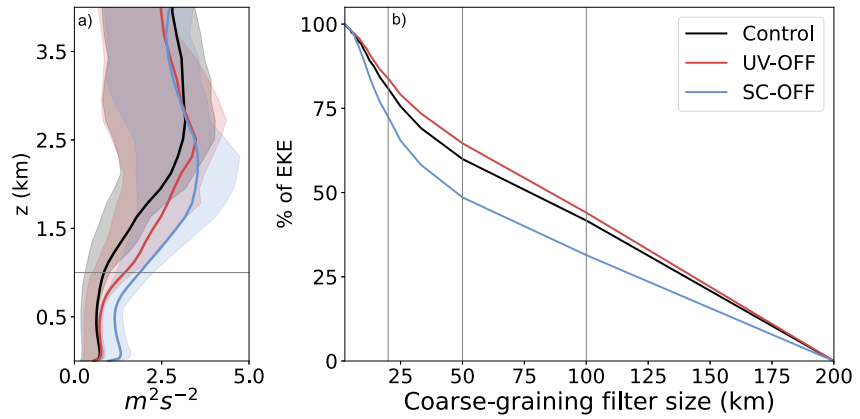


**Figure 8.** Eddy kinetic energy (EKE) as a proxy of mesoscale wind variability. Panel (a) shows the mean profile and interquartile range (shaded) of EKE, without any coarsening. Panel (b) shows the percentage of EKE at 1 km height (indicated by the horizontal gray line in panel a) for progressively coarser filter sizes. The vertical gray lines indicate filters of 20, 50, and 100 km. Black is for the control, red for UV-OFF, and blue for SC-OFF.

shear production. Zonal shear production of EKE is the largest term for all experiments, with a peak around 2 km near the inversion, where wind shear and resolved momentum fluxes (Figure 7g) peak.

In SC-OFF (blue) zonal shear production of EKE is, on average, twice as large due to stronger  $w'_{res}$ , except near 1 km, where a local wind maximum leads to small shear  $\frac{\partial \bar{u}}{\partial z} \approx 0$  (see Figure 2c). The meridional shear production of EKE is also larger than the control for both SC-OFF and UV-OFF, peaking near 1.5 km in SC-OFF and just above 1 km in UV-OFF. In other words, parameterized momentum transport by SC in the control is effective at diffusing EKE that is established in the cloud layer on mesoscales.

Eddy kinetic energy production is anisotropic, with buoyancy production occurring only in the vertical component  $w$ . The EKE anisotropy, expressed as  $\sigma_w^2/(\sigma_u^2 + \sigma_v^2)$  in Figure 9d (Section 3.3) helps quantify the

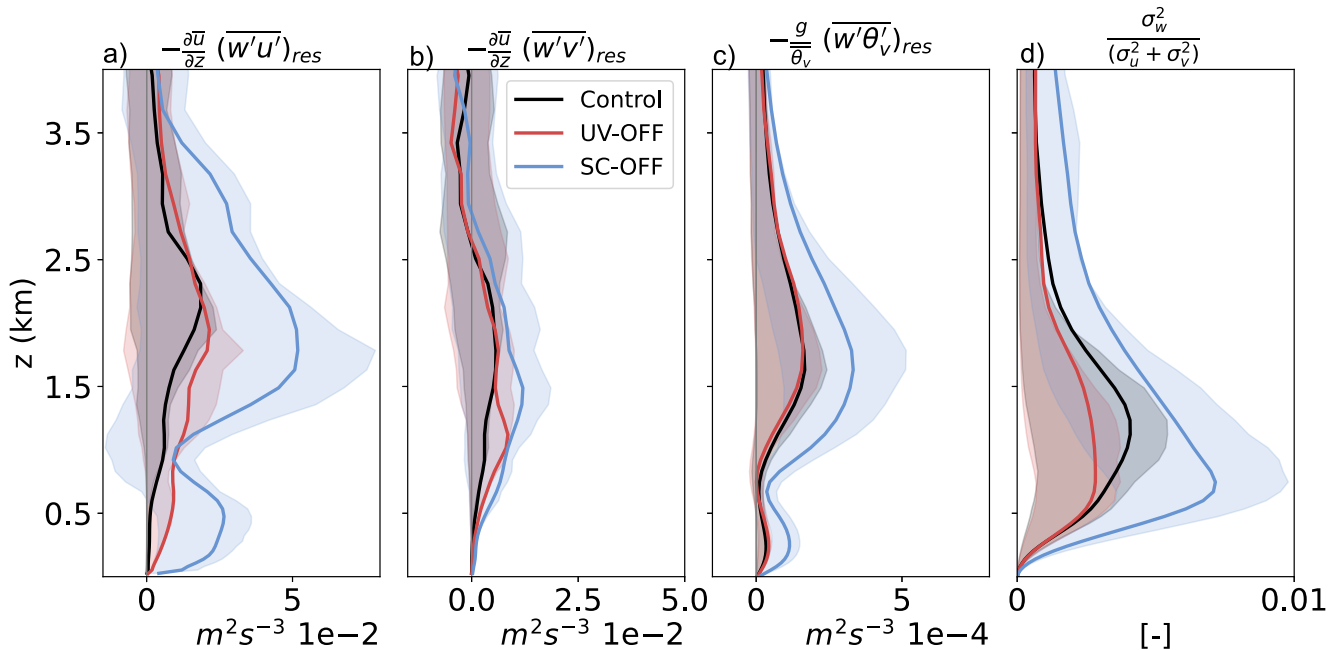


**Figure 9.** Source (or sink) terms of eddy kinetic energy EKE: (a) zonal shear production  $-\frac{\partial \bar{u}}{\partial z} (\overline{w'u'})_{res}$ , (b) meridional shear production  $-\frac{\partial \bar{v}}{\partial z} (\overline{w'v'})_{res}$ , and (c) buoyancy production  $-\frac{g}{\theta_v} (\overline{w'\theta'_v})_{res}$ . In panel (d) is the non-dimensional term  $\sigma_w^2/(\sigma_u^2 + \sigma_v^2)$ , which quantifies EKE anisotropy. The fluxes and the variances ( $\sigma_u^2$ ,  $\sigma_v^2$ ,  $\sigma_w^2$ ) refer to scales larger than 2.5 km.

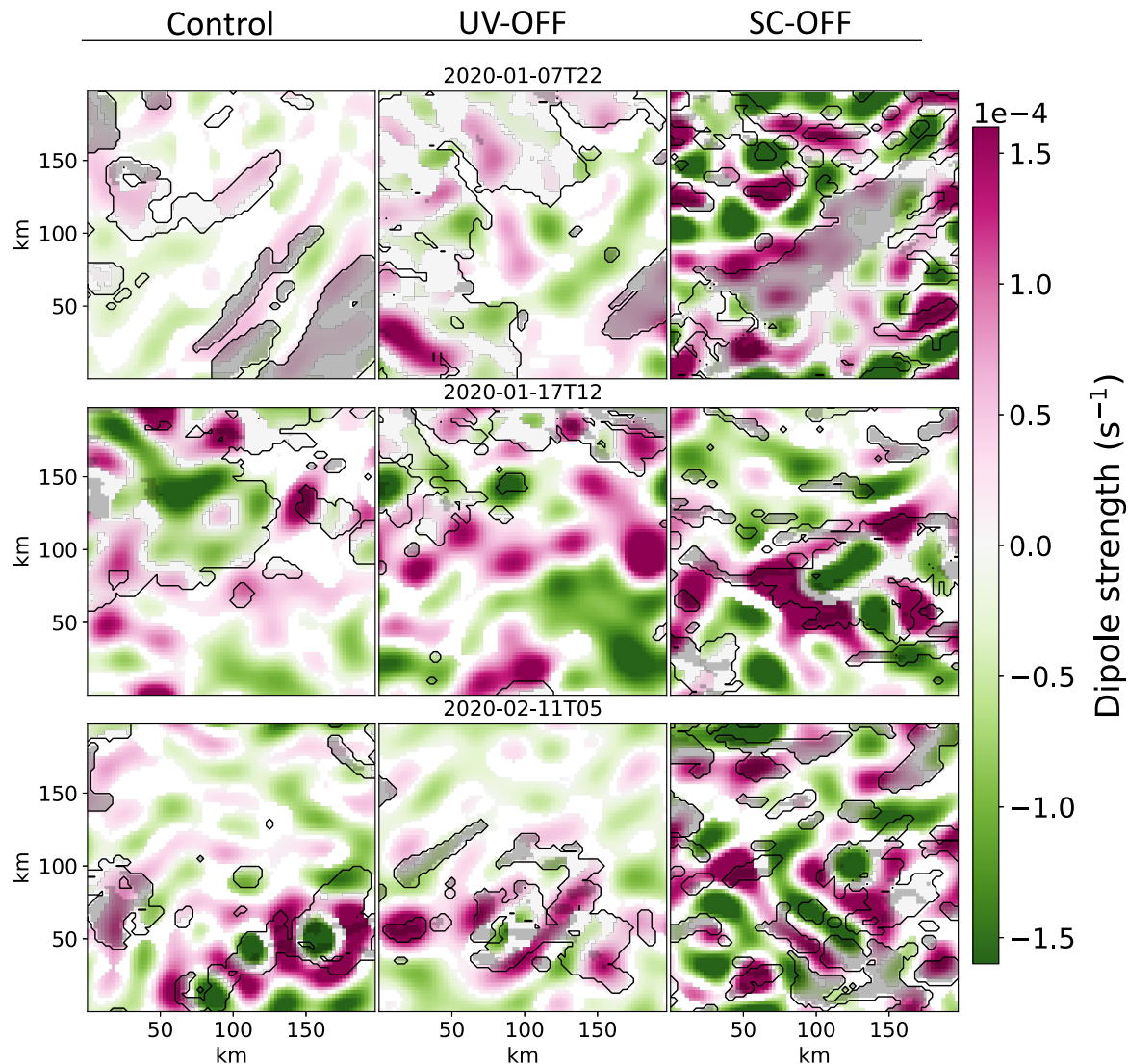


**Figure 10.** Instantaneous fields of dipole  $D'$  strength, defined as the delta between the sub-cloud and the cloud layer divergence  $D$ . Positive (negative) values indicate sub-cloud layer convergence (divergence). The black contours and the gray shading indicate cloudy grids. Light (dark) shading is for grids with cloud base above (below) 1 km. Each row refers to a date (7 January at 22:00 LT, 17 January at 12:00 LT, and 11 February at 05:00 LT), each column refers to an experiment.

relatively importance of buoyancy versus shear (Salesky et al., 2017). The EKE anisotropy is largest in the cloud layer, and it increases from the control to the SC-OFF experiment, suggesting a relative larger increase in buoyancy production compared to shear production. The response is opposite in UV-OFF (red), where the mean EKE anisotropy decreases in the cloud layer compared to the control. This is explained by more shear production (panels a and b) and almost equal buoyancy production (panel c) to the control.

## 7. Mesoscale Circulations

Following George et al. (2023), we introduced a definition of mesoscale overturning circulations (SMOCs) in Section 3.3, which are regions where the sub-cloud and the cloud layers exhibit mesoscale horizontal divergence  $D$  with the opposite sign. The  $D$  dipole ( $D'$ ) is positive when mesoscale ascent leads to divergence in the cloud layer and convergence in the sub-cloud layer, and vice-versa, negative for mesoscale subsidence.

Figure 10 shows SMOCs colored by  $D'$  so that positive values (magenta) indicate convergence in the sub-cloud layer, and negative values (green) indicate divergence in the sub-cloud layer. White indicates areas with  $|D| < 10^{-6} \text{ s}^{-1}$  (see Section 3.3 about the threshold) or areas where divergence in the sub-cloud and cloud layers

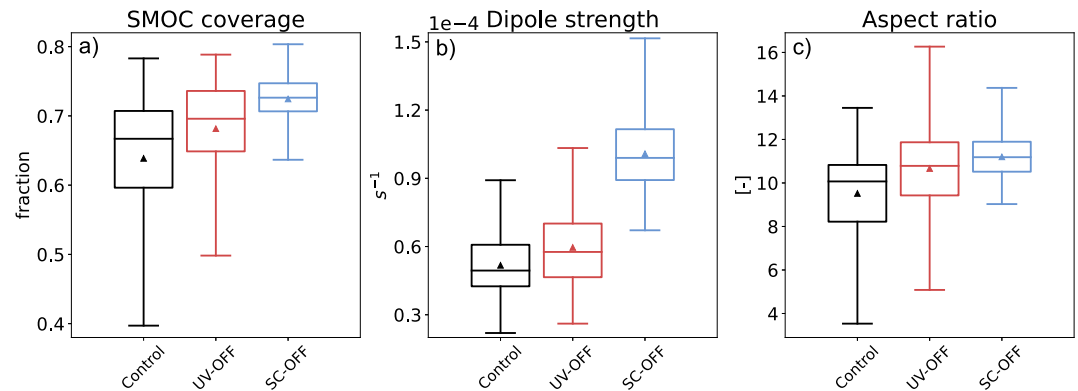


**Figure 11.** Panel (a) shows the distribution of SMOC coverage, defined as the area fraction covered by SMOCs. Panel (b) shows the SMOC strength, defined as the magnitude of the dipole  $D'$  of mesoscale horizontal wind divergence. Panel (c) shows the non-dimensional aspect ratio of SMOCs, defined as the ratio between horizontal size and vertical extent. Box limits indicate the interquartile range, with a central line marking the median. The triangle indicates the mean, and the whiskers capture the range of the remaining data.

have the same sign (no dipole). The cloud field is also shown on top as gray shading, where the light shading indicates cloudy columns with a cloud base above 1 km, and darker shading is for cloudy columns with a cloud base below 1 km. The three examples include: 7 January at 22:00 LT (top row), when both UV-OFF and SC-OFF produce larger CC than the control ( $CC_{\text{control}} = 0.26$ ,  $CC_{\text{UV-OFF}} = 0.51$ ,  $CC_{\text{SC-OFF}} = 0.55$ ); 17 January at 12:00 LT (middle row), when UV-OFF and SC-OFF both produce smaller CC than the control ( $CC_{\text{control}} = 0.42$ ,  $CC_{\text{UV-OFF}} = 0.19$ ,  $CC_{\text{SC-OFF}} = 0.29$ ); and 11 February at 05:00 LT (bottom row), when  $CC_{\text{control}} = 0.19$ ,  $CC_{\text{UV-OFF}} = 0.17$ ,  $CC_{\text{SC-OFF}} = 0.31$ .

In all three experiments, SMOCs are prevalent, as in the observations (George et al., 2023), with alternating (in space) converging and diverging branches of circulations. Convergence and divergence, and thus the dipole  $D'$ , are generally stronger when convection is resolved for example, SC-OFF in the right column, which highlights the coupling between convection and mesoscale wind fields. Just from visual inspection, clouds in some scenes seem to favor regions of strong convergence/divergence (see the bottom row for control and UV-OFF), but even in regions without clouds, or where clouds are not rooted below 1 km, SMOCs are evident. We return to the relationship between cloudiness and circulations in Section 8 below.

In Figure 11 we quantify the area covered by SMOCs in panel (a), the strength of  $D'$  in (b) and the horizontal-to-vertical aspect ratio of SMOCs in (c). Removing parameterized transport from control to UV-OFF and then to SC-OFF incrementally increases the coverage and strength of SMOCs. The SMOC coverage increases from  $\sim 0.65$  in the control to more than 0.7 in SC-OFF, with explicit convection strongly narrowing the distribution at the lower end (scenes without SMOCs become rare). The strength is about  $0.5 \times 10^{-4}$  in the control,  $0.6 \times 10^{-4}$  in UV-OFF, and  $1 \times 10^{-4}$  in SC-OFF. The increase in SMOC strength is in line with our analysis of EKE.

The aspect ratio in Figure 11c indicates how much wider than taller the SMOCs are. The mean boundary layer height that effectively sets the vertical extent of SMOCs (defined in Section 3.3) is between 1 and 1.5 km throughout the simulated period and does not differ much between the experiments. The mean horizontal size of SMOCs varies more, with most values between 10 and 16 km, leading to a mean aspect ratio around 10. In the control (black) the aspect ratio ranges between 4 and 14, while for SC-OFF (blue) it is never lower than 8. In UV-OFF (red) the largest aspect ratios are found, up to 16, but a long tail toward low aspect ratios keeps the mean ratio small.

## 8. Relation Between Changes in Cloudiness and Circulations

Whether clouds drive mesoscale circulations or vice-versa is an ongoing topic of discussion in the community. According to George et al. (2023), SMOCs are not likely driven by radiation; instead, they are thought to be sustained or enhanced by moisture anomalies in the sub-cloud layer. Jansson et al. (2023) reveal how such moisture anomalies can grow from the initial (latent) heating perturbations produced by shallow cumulus



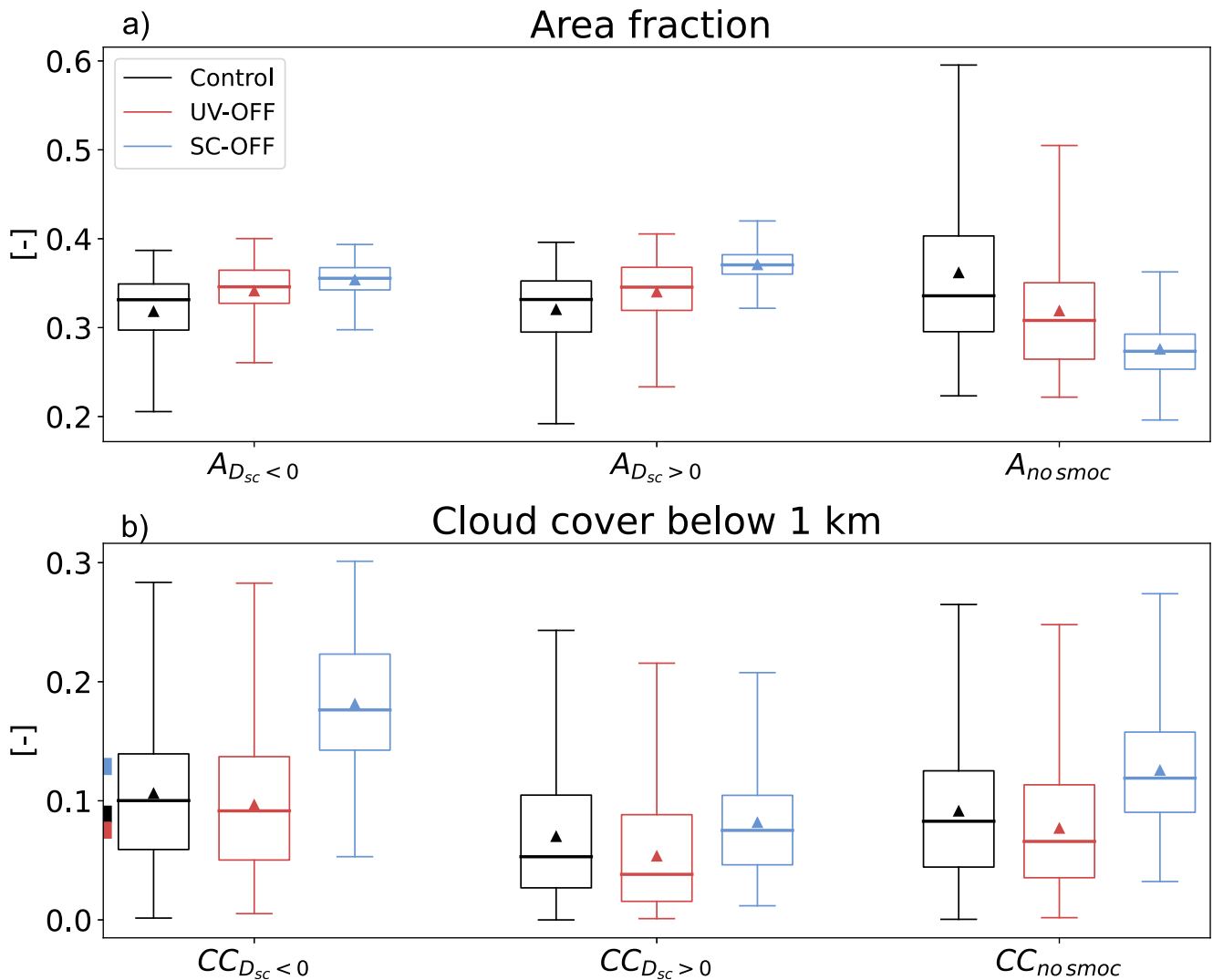


**Figure 12.** In (a) the area covered by converging SMOCs, diverging SMOCs, and the area without SMOCs (*no smoc*) are shown for the control, UV-OFF, and SC-OFF. In (b), cloud cover below 1 km is shown, sampled on the area covered by converging SMOCs ( $CC_{D_{sc} < 0}$ ), the area covered by diverging SMOCs ( $CC_{D_{sc} > 0}$ ), and the area not on SMOCs ( $CC_{no\ smoc}$ ). The square markers on the left y-axis are the mean CC below 1 km sampled on the entire domain as in Figure 5 ( $CC_{z < 1km}$ ).

convection. One of our questions is whether changes in the circulations between the control and other experiments help explain the overall changes in low cloud cover, in particular the increase in  $CC_{z < 1km}$  from the control to the SC-OFF experiment, and the small decrease in  $CC_{z < 1km}$  from the control to UV-OFF (Figure 5).

Figure 10 suggests that SMOCs are more ubiquitous than clouds, that is, not all converging SMOCs exhibit clouds. Figure 11a indeed shows that SMOCs cover a much larger fraction of the domain ( $\sim 0.7$ ) compared to the fraction covered by clouds below 1 km ( $\sim 0.1$ ) (Figure 5).

To address whether clouds are favored over converging SMOCs we divide the distribution of SMOC coverage in Figure 11a into areas of sub-cloud convergence, divergence or neither (*no smoc*), the sum of which equals 1. The increase in SMOC coverage in SC-OFF and UV-OFF as seen in Figure 11 evidently comes from an increase in both converging and diverging branches, while areas with no SMOCs become rare.

In UV-OFF, changes in resolved updraft strength  $w^{UP}$  (Figure 3), in the heat flux, and thermodynamic profiles are marginal, so that we expect that changes in cloud statistics are produced through changes in the dynamics. In the absence of parameterized wind mixing between converging and diverging layers, stronger and more extensive



SMOCs regions can be sustained. This condition suggests more stratiform cloudiness in a cloud layer confined by the trade-inversion, at times when SMOCs are promoted.

In Figure 12b we show CC below 1 km sampled over only the converging branches of SMOCs where  $D_{sc} < 0$ , or only the diverging branch where  $D_{sc} > 0$ , and only over the areas with no meaningful SMOC dipole (*no smoc*). For completeness we also show, as square markers on the left y-axis, the mean cloud cover ( $CC_{z < 1km}$ ) over the entire domain, derived from Figure 5. Summing the product of area fraction times the cloud cover over these different categories would give the total (domain) cloud cover.

Clouds are found preferentially in areas of sub-cloud convergence. In all three experiments,  $CC_{D_{sc} < 0}$  is higher than the overall CC, and higher than over areas with sub-cloud divergence or areas without SMOCs. The difference is most pronounced with fully explicit resolved convection in SC-OFF. Mean values for CC are around 0.1 for the control and UV-OFF, and 0.17 for SC-OFF over converging SMOCs. The lowest cloud cover is found over diverging SMOCs, where 50% of the time cloud cover is below 0.05 in the control and in the UV-OFF experiment. Regions where no SMOCs are detected have a CC distribution that represents well the domain average, with mean values around 0.08 for the control and UV-OFF, and 0.13 for SC-OFF. The results show that the enhanced cloudiness in SC-OFF is dominated by enhanced cloudiness above converging SMOCs, whereas the reduced cloudiness in UV-OFF is dominated by reduced cloudiness above diverging SMOCs and *no smoc* regions.

## 9. Conclusions

This study investigates the influence of parameterized and resolved shallow convective transport on the cloud field and on mesoscale circulations using the mesoscale model HARMONIE-AROME. The model experiments focus on the EUREC4A-MIP, simulating a large domain east of Barbados over the north Atlantic trade-wind region from 1 January to 29 February 2020. Three model simulations are carried out: (a) a control simulation with an active SCP; (b) an experiment without parameterized momentum transport by shallow convection, UV-OFF; (c) an experiment with an inactive SCP, thus omitting all parameterized transport by shallow convection, SC-OFF. The goal is to shed light on the implications of parameterized shallow convection in kilometer-scale simulations and evaluate our conceptual understanding of mesoscale cloud organization and circulations coupled to shallow convection.

In the UV-OFF and SC-OFF experiments, the missing parameterized transport of momentum in the sub-cloud layer is almost entirely compensated by an increase in momentum transport by the eddy-diffusivity scheme, in response to stronger wind shear developing. In the cloud layer, resolved convection only partially takes over the momentum transport. In SC-OFF, the total heat and moisture fluxes increase, carried by much stronger convection now resolved at the grid-scale.

Inspired by (Honnert et al., 2011), we recently performed 10 days of large-eddy simulations with 100 m grid spacing over a  $150 \times 150$  km domain for the same EUREC4A period (Savazzi et al., 2024) to study, among other things, the dependence of total turbulent flux on grid spacing. At a grid spacing of 2.5 km, the sub-grid heat and moisture flux should carry more than 60% of the total flux in the middle of the cloud layer. This is far from being the case for the SC-OFF experiment, where the resolved fluxes largely dominate the sub-grid fluxes from the ED scheme (Figure 7). In the control experiment, the partition between sub-grid and resolved fluxes is more similar to what is suggested by LES.

With a grid spacing of 2.5 km, the non-local transport of heat and moisture from the lower to the upper cloud layer is more efficient when done by resolved eddies in SC-OFF than by the parameterization in the control. In contrast, the sub-cloud layer is less efficiently mixed by resolved eddies, highlighting the importance of the parameterized dry mass-flux transport. Removing sub-grid transport by SC effectively builds up instability in the lower layers and triggers strong resolved updrafts.

Compared to satellite infrared imagery (GOES16), the SC-OFF experiment, with stronger convection, degrades the structure and organization of the projected cloud field. Clouds become too deep and are too small and numerous. They are also distributed too uniformly across the domain, reducing the fraction of open sky, and become more symmetric. The larger number of clouds increases cloud cover below 1 km. A few of these clouds rise deeper driven by strong updrafts, resulting in more precipitation. As convection is deeper and mixing is more

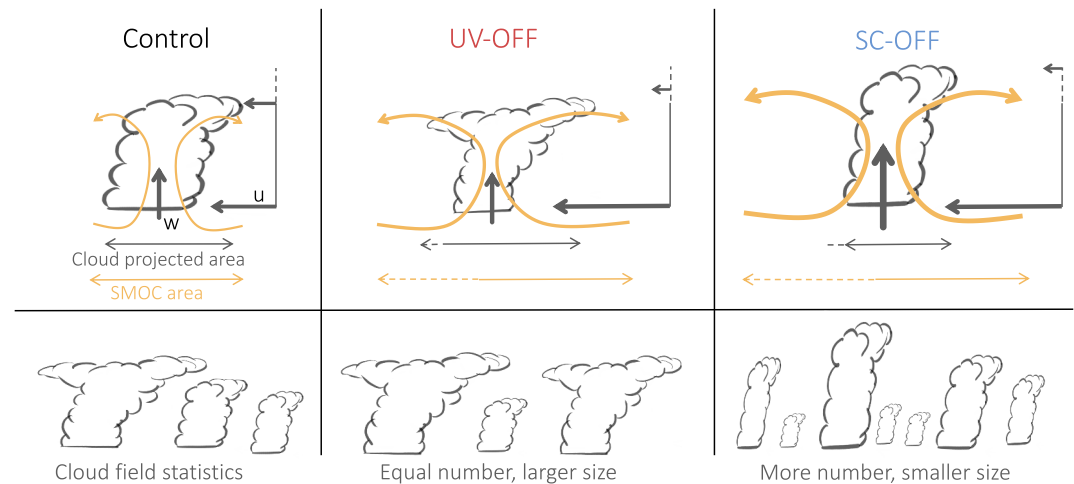


**Figure 13.** Sketch representing, for the three experiments, a typical resolved mesoscale circulation (top row) and a typical cloud field (bottom row).

efficient in the cloud layer, the inversion is weaker and widespread stratiform outflow layers below the inversion are less common, reducing cloud cover above 1 km. Radiosonde measurements further reveal that in the SC-OFF (and in UV-OFF) a too strong zonal wind jet develops near cloud base.

In SC-OFF, larger total heat fluxes driven by stronger resolved convection (leading to larger resolved eddy kinetic energy) strengthen and widen the areas with significant mesoscale convergence and divergence. While the increased wind shear works against convection (Helfer et al., 2020), changes in the thermodynamic environment outclass the shear effect and shallow meridional overturning circulations (George et al., 2023), or SMOCs, become more pronounced (Figure 13).

The UV-OFF experiment develops larger eddy kinetic energy in the cloud layer due to less sub-grid momentum mixing in this layer and thus more horizontal wind variance. Shallow mesoscale overturning circulations become somewhat stronger and wider. This is favorable for cloudiness that forms in the upper cloud layer, as UV-OFF produces larger clouds above 1 km, due to more or wider stratiform outflow layers (Figure 13).

The extent to which the ED scheme and the resolved flow can compensate for the missing transport by SCP is dependent on the model resolution. Interestingly, removing the SCP in a coarser model, like IFS (ECMWF, 2024) with ~9 km grid spacing, produces an opposite response from that in HARMONIE. In the IFS, SMOCs are hardly resolved and resolved motions do not effectively take over the parameterized transport by SC. This leads to a lack of vertical mixing when removing the SCP in IFS, increasing the stability and strengthening the inversion (Bechtold et al., 2014). Other components of the model, such as the cloud scheme, could also influence this response, although less pronouncedly as resolution refines. Despite the many pitfalls (Brown et al., 2006; Schlemmer et al., 2017; Xiao et al., 2023), our results demonstrate that even at a grid spacing of 2.5 km, a parameterization for shallow convection may be needed.

## Data Availability Statement

The data from the three HARMONIE-AROME experiments used in this study are publicly available at the following DOI: 10.4121/d61e2238-b969-45e1-8649-62197f30025a with CC BY-SA (Savazzi & de Rooy, 2024). All observational data used in this study are freely available and can be easily accessed via the EUREC4A-Intake catalogue at <https://github.com/eurec4a/eurec4a-intake> (community, 2023) as described at [howto.eurec4a.eu](https://howto.eurec4a.eu).

## Acknowledgments

This project has received funding from the Dutch Research Council (NWO) VIDI CMTRACE (Starting Grant Agreement VI.Vidi.192.050). The authors thank Bert van Ulft for helping to set up the model experiments and Gheylla Liberia for an insightful first analysis of the data set. The authors would also like to thank the three anonymous reviewers for the time they spent reviewing the manuscript. Their comments and suggestions have contributed to improving the quality of this study.

## References

- Agee, E. M., Chen, T. S., & Dowell, K. E. (1973). A review of mesoscale cellular convection. *Bulletin of the American Meteorological Society*, 54(10), 1004–1012. [https://doi.org/10.1175/1520-0477\(1973\)054<1004:aromcc>2.0.co;2](https://doi.org/10.1175/1520-0477(1973)054<1004:aromcc>2.0.co;2)
- Arakawa, A., Jung, J.-H., & Wu, C.-M. (2011). Toward unification of the multiscale modeling of the atmosphere. *Atmospheric Chemistry and Physics*, 11(8), 3731–3742. <https://doi.org/10.5194/acp-11-3731-2011>
- Atkinson, B. W., & Wu Zhang, J. (1996). Mesoscale shallow convection in the atmosphere. *Reviews of Geophysics*, 34(4), 403–431. <https://doi.org/10.1029/96RG02623>
- Bechtold, P., Cuijpers, J. W. M., Mascart, P., & Trouillet, P. (1995). Modeling of trade wind cumuli with a low-order turbulence model: Toward a unified description of Cu and Sc clouds in meteorological models. *Journal of the Atmospheric Sciences*, 52(4), 455–463. [https://doi.org/10.1175/1520-0469\(1995\)052<0455:mtwcw>2.0.co;2](https://doi.org/10.1175/1520-0469(1995)052<0455:mtwcw>2.0.co;2)
- Bechtold, P., Sandu, I., Klocke, D., Semane, N., Ahlgrimm, M., Beljaars, A., et al. (2014). The role of shallow convection in ECMWF's integrated forecasting system. *ECMWF*. <https://doi.org/10.21957/heba1qwm>
- Bengtsson, L., Andrae, U., Aspelien, T., Batrak, Y., Calvo, J., Rooy, W. d., et al. (2017). The HARMONIE AROME model configuration in the ALADIN HIRLAM NWP system. *Monthly Weather Review*, 145(5), 1919–1935. <https://doi.org/10.1175/MWR-D-16-0417.1>
- Boing, S. J., Siebesma, A. P., Korpershoek, J. D., & Jonker, H. J. J. (2012). Detrainment in deep convection. *Geophysical Research Letters*, 39(20). <https://doi.org/10.1029/2012GL053735>
- Bony, S., Schulz, H., Vial, J., & Stevens, B. (2020a). Sugar, gravel, fish, and flowers: Dependence of mesoscale patterns of trade-wind clouds on environmental conditions. *Geophysical Research Letters*, 47(7), e2019GL085988. <https://doi.org/10.1029/2019GL085988>
- Bony, S., Semie, A., Kramer, R. J., Soden, B., Tompkins, A. M., & Emanuel, K. A. (2020b). Observed modulation of the tropical radiation budget by deep convective organization and lower-tropospheric stability. *AGU Advances*, 1(3), e2019AV000155. <https://doi.org/10.1029/2019AV000155>
- Bougeault, P. (1981). Modeling the trade-wind cumulus boundary layer. Part I: Testing the ensemble cloud relations against numerical data. *Journal of the Atmospheric Sciences*, 38(11), 2414–2428. [https://doi.org/10.1175/1520-0469\(1981\)038<2414:mtwcw>2.0.co;2](https://doi.org/10.1175/1520-0469(1981)038<2414:mtwcw>2.0.co;2)
- Boutle, I. A., Eyre, J. E. J., & Lock, A. P. (2014). Seamless stratocumulus simulation across the turbulent gray zone. *Monthly Weather Review*, 142(4), 1655–1668. <https://doi.org/10.1175/MWR-D-13-00229.1>
- Brast, M., Schemann, V., & Neggers, R. A. J. (2018). Investigating the scale adaptivity of a size-filtered mass flux parameterization in the gray zone of shallow cumulus convection. *Journal of the Atmospheric Sciences*, 75(4), 1195–1214. <https://doi.org/10.1175/JAS-D-17-0231.1>
- Brown, A. R., Beljaars, A. C. M., & Hersbach, H. (2006). Errors in parametrizations of convective boundary-layer turbulent momentum mixing. *Quarterly Journal of the Royal Meteorological Society*, 132(619), 1859–1876. <https://doi.org/10.1256/qj.05.182>
- Bryan, G. H., Wyngaard, J. C., & Fritsch, J. M. (2003). Resolution requirements for the simulation of deep moist convection. *Monthly Weather Review*, 131(10), 2394–2416. [https://doi.org/10.1175/1520-0493\(2003\)131\(2394:RRFTSO\)2.0.CO;2](https://doi.org/10.1175/1520-0493(2003)131(2394:RRFTSO)2.0.CO;2)
- community, E. (2023). EUREC4A (version 1). *Zenodo*. [Dataset]. <https://doi.org/10.5281/zenodo.8422322>
- Craig, G. C., & Dornbrack, A. (2008). Entrainment in cumulus clouds: What resolution is cloud-resolving? *Journal of the Atmospheric Sciences*, 65(12), 3978–3988. <https://doi.org/10.1175/2008JAS2613.1>
- de Rooy, W. C., Bechtold, P., Frohlich, K., Hohenegger, C., Jonker, H., Mironov, D., et al. (2013). Entrainment and detrainment in cumulus convection: An overview. *Quarterly Journal of the Royal Meteorological Society*, 139(670), 1–19. <https://doi.org/10.1002/qj.1959>
- de Rooy, W. C., & Siebesma, A. (2010). Analytical expressions for entrainment and detrainment in cumulus convection. *Quarterly Journal of the Royal Meteorological Society*, 136(650), 1216–1227. <https://doi.org/10.1002/qj.640>
- de Rooy, W. C., & Siebesma, A. P. (2008). A simple parameterization for detrainment in shallow cumulus. *Monthly Weather Review*, 136(2), 560–576. <https://doi.org/10.1175/2007MWR2201.1>
- de Rooy, W. C., Siebesma, P., Baas, P., Lenderink, G., de Roode, S. R., de Vries, H., et al. (2022). Model development in practice: A comprehensive update to the boundary layer schemes in HARMONIE-AROME cycle 40. *Geoscientific Model Development*, 15(4), 1513–1543. <https://doi.org/10.5194/gmd-15-1513-2022>
- Dorrestijn, J., Crommelin, D. T., Siebesma, A. P., & Jonker, H. J. J. (2013). Stochastic parameterization of shallow cumulus convection estimated from high-resolution model data. *Theoretical and Computational Fluid Dynamics*, 27(1), 133–148. <https://doi.org/10.1007/s00162-012-0281-y>
- ECMWF. (2024). IFS documentation. *Cycles 47r3 to 48r1 [Manual]*. Retrieved from <https://www.ecmwf.int/en/forecasts/documentation-and-support/changes-ecmwf-model>
- George, G., Stevens, B., Bony, S., Pincus, R., Fairall, C., Schulz, H., et al. (2021). Joanne : Joint dropsonde observations of the atmosphere in tropical North atlantic meso-scale environments. *Earth System Science Data Discussions*, 1–33. <https://doi.org/10.5194/essd-2021-162>
- George, G., Stevens, B., Bony, S., Vogel, R., & Naumann, A. K. (2023). Widespread shallow mesoscale circulations observed in the trades. *Nature Geoscience*, 16(7), 584–589. <https://doi.org/10.1038/s41561-023-01215-1>
- Golaz, J.-C., Larson, V. E., & Cotton, W. R. (2002). A PDF-based model for boundary layer clouds. Part I: Method and model description. *Journal of the Atmospheric Sciences*, 59(24), 3540–3551. [https://doi.org/10.1175/1520-0469\(2002\)059<3540:apbmfb>2.0.co;2](https://doi.org/10.1175/1520-0469(2002)059<3540:apbmfb>2.0.co;2)
- Helffer, K. C., Nuijens, L., Roode, S. R. D., & Siebesma, P. (2020). How wind shear affects trade-wind cumulus convection. [preprint]. <https://doi.org/10.1002/essoar.10503170.1>
- Hersbach, H., Bell, B., Berrisford, P., Hirahara, S., Horányi, A., Muñoz-Sabater, J., et al. (2020). The ERA5 global reanalysis. *Quarterly Journal of the Royal Meteorological Society*, 146(730), 1999–2049. <https://doi.org/10.1002/qj.3803>
- Holland, J. Z., & Raschusson, E. M. (1973). Measurements of the atmospheric mass, energy, and momentum budgets over a 500-kilometer square of tropical ocean. *Monthly Weather Review*, 101(1), 44–55. [https://doi.org/10.1175/1520-0493\(1973\)101\(0044:MOTAME\)2.3.CO;2](https://doi.org/10.1175/1520-0493(1973)101(0044:MOTAME)2.3.CO;2)
- Honnert, R. (2019). Grey-zone turbulence in the neutral atmospheric boundary layer. *Boundary-Layer Meteorology*, 170(2), 191–204. <https://doi.org/10.1007/s10546-018-0394-y>
- Honnert, R., Masson, V., & Couvreux, F. (2011). A diagnostic for evaluating the representation of turbulence in atmospheric models at the kilometric scale. *Journal of the Atmospheric Sciences*, 68(12), 3112–3131. <https://doi.org/10.1175/JAS-D-11-061.1>
- Janssens, M., Arellano, J. V.-G. d., Heerwaarden, C. C. v., Roode, S. R. d., Siebesma, A. P., & Glassmeier, F. (2022). Non-precipitating shallow cumulus convection is intrinsically unstable to length-scale growth. *Journal of the Atmospheric Sciences*, 1(aop). <https://doi.org/10.1175/JAS-D-22-0111.1>
- Janssens, M., Arellano, J. V.-G. d., Scheffer, M., Antonissen, C., Siebesma, A. P., & Glassmeier, F. (2021). Cloud patterns in the trades have four interpretable dimensions. *Geophysical Research Letters*, 48(5), e2020GL091001. <https://doi.org/10.1029/2020GL091001>
- Jansson, F., Janssens, M., Grönqvist, J. H., Siebesma, A. P., Glassmeier, F., Attema, J., et al. (2023). Cloud Botany: Shallow cumulus clouds in an ensemble of idealized large-domain large-eddy simulations of the trades. *Journal of Advances in Modeling Earth Systems*, 15(11), e2023MS003796. <https://doi.org/10.1029/2023MS003796>

- Jonker, H. J., Verzijlbergh, R. A., Heus, T., & Siebesma, A. P. (2006). The influence of the sub-cloud moisture field on cloud size distributions and the consequences for entrainment. In *17th symposium on boundary layers and turbulence, 27th conference on agricultural and forest meteorology, 17th conference on biometeorology and aerobiology*. Retrieved from [https://engagedscholarship.csuohio.edu/sciphysics\\_facpub/427](https://engagedscholarship.csuohio.edu/sciphysics_facpub/427)
- Kurowski, M. J., Paris, A., & Teixeira, J. (2024). The unique behavior of vertical velocity in developing deep convection. *Geophysical Research Letters*, 51(20), e2024GL110425. <https://doi.org/10.1029/2024GL110425>
- Lamaakel, O., & Matheou, G. (2022). Organization development in precipitating shallow cumulus convection: Evolution of turbulence characteristics. *Journal of the Atmospheric Sciences*, 79(9), 2419–2433. <https://doi.org/10.1175/JAS-D-21-0334.1>
- Lancz, D., Szintai, B., & Honnert, R. (2018). Modification of a parametrization of shallow convection in the grey zone using a mesoscale model. *Boundary-Layer Meteorology*, 169(3), 483–503. <https://doi.org/10.1007/s10546-018-0375-1>
- Larson, V. E., Domke, S., & Griffin, B. M. (2019). Momentum transport in shallow cumulus clouds and its parameterization by higher-order closure. *Journal of Advances in Modeling Earth Systems*, 11(11), 3419–3442. <https://doi.org/10.1029/2019MS001743>
- LeMone, M. A., Barnes, G. M., & Zipser, E. J. (1984). Momentum flux by lines of cumulonimbus over the tropical oceans. *Journal of the Atmospheric Sciences*, 41(12), 1914–1932. [https://doi.org/10.1175/1520-0469\(1984\)041<1914:MFBLOC>2.0.CO;2](https://doi.org/10.1175/1520-0469(1984)041<1914:MFBLOC>2.0.CO;2)
- Malkus, J. S., & Riehl, H. (1964). Cloud structure and distributions over the tropical Pacific Ocean I. *Tellus*, 16(3), 275–287. <https://doi.org/10.1111/j.2153-3490.1964.tb00167>
- Marchand, R., Ackerman, T., Smyth, M., & Rossow, W. B. (2010). A review of cloud top height and optical depth histograms from MISR, ISCCP, and MODIS. *Journal of Geophysical Research*, 115(D16). <https://doi.org/10.1029/2009JD013422>
- Neggers, R. A. J. (2009). A dual mass flux framework for boundary layer convection. Part II: Clouds. *Journal of the Atmospheric Sciences*, 66(6), 1489–1506. <https://doi.org/10.1175/2008JAS2636.1>
- NOAA. (2020). GOES-R series data book. Retrieved from <https://www.goes-r.gov>
- Nuijens, L., Serikov, I., Hirsch, L., Lonitz, K., & Stevens, B. (2014). The distribution and variability of low-level cloud in the North Atlantic trades. *Quarterly Journal of the Royal Meteorological Society*, 140(684), 2364–2374. <https://doi.org/10.1002/qj.2307>
- Petch, J. C., Brown, A. R., & Gray, M. E. B. (2002). The impact of horizontal resolution on the simulations of convective development over land. *Quarterly Journal of the Royal Meteorological Society*, 128(584), 2031–2044. <https://doi.org/10.1256/003590002320603511>
- Radtke, J., Naumann, A. K., Hagen, M., & Ament, F. (2022). The relationship between precipitation and its spatial pattern in the trades observed during EUREC4A. *Quarterly Journal of the Royal Meteorological Society*, 148(745), 1913–1928. <https://doi.org/10.1002/qj.4284>
- Rasp, S., Schulz, H., Bony, S., & Stevens, B. (2020). Combining crowdsourcing and deep learning to explore the mesoscale organization of shallow convection. *Bulletin of the American Meteorological Society*, 101(11), E1980–E1995. <https://doi.org/10.1175/BAMS-D-19-0324.1>
- Rauber, R. M., Stevens, B., Ochs, H. T., Knight, C., Albrecht, B. A., Blyth, A. M., et al. (2007). Rain in shallow cumulus over the ocean: The RICO campaign. *Bulletin of the American Meteorological Society*, 88(12), 1912–1928. <https://doi.org/10.1175/BAMS-88-12-1912>
- Rio, C., & Hourdin, F. (2008). A thermal plume model for the convective boundary layer: Representation of cumulus clouds. *Journal of the Atmospheric Sciences*, 65(2), 407–425. <https://doi.org/10.1175/2007JAS2256.1>
- Salesky, S. T., Chamecki, M., & Bou-Zeid, E. (2017). On the nature of the transition between roll and cellular organization in the convective boundary layer. *Boundary-Layer Meteorology*, 163(1), 41–68. <https://doi.org/10.1007/s10546-016-0220-3>
- Sandu, I., Bechtold, P., Nuijens, L., Beljaars, A., & Brown, A. (2020). On the causes of systematic forecast biases in near-surface wind direction over the oceans. *ECMWF Technical Memorandum*, 866. <https://doi.org/10.21957/wggbl43u>
- Savazzi, A., & de Rooy, W. (2024). Data from the study on the influence of parameterised shallow convection on trade-wind clouds and circulations in the HARMONIE-AROME mesoscale model (Version 1). *ResearchData*. [Dataset]. 4TU. <https://doi.org/10.4121/D61E2238-B969-45E1-8649-62197F30025A.V1>
- Savazzi, A., Nuijens, L., Rooy, W. d., Janssens, M., & Siebesma, A. P. (2024). Momentum transport in organized shallow cumulus convection. *Journal of the Atmospheric Sciences*, 81(2), 279–296. <https://doi.org/10.1175/JAS-D-23-0098.1>
- Savazzi, A., Nuijens, L., Sandu, I., George, G., & Bechtold, P. (2022). The representation of the trade winds in ECMWF forecasts and reanalyses during EUREC4A. *Atmospheric Chemistry and Physics*, 22(19), 13049–13066. <https://doi.org/10.5194/acp-22-13049-2022>
- Schlemmer, L., Bechtold, P., Sandu, I., & Ahlgrim, M. (2017). Uncertainties related to the representation of momentum transport in shallow convection. *Journal of Advances in Modeling Earth Systems*, 9(2), 1269–1291. <https://doi.org/10.1002/2017MS000915>
- Schneider, T., Teixeira, J., Bretherton, C. S., Brient, F., Pressel, K. G., Schar, C., & Siebesma, A. P. (2017). Climate goals and computing the future of clouds. *Nature Climate Change*, 7(1), 3–5. <https://doi.org/10.1038/nclimate3190>
- Schulz, H. (2022). C<sup>3</sup>ONTEXT: A common consensus on convective OrganizaTion during the EUREC4A eXperiment. *Earth System Science Data*, 14(3), 1233–1256. <https://doi.org/10.5194/essd-14-1233-2022>
- Sherwood, S. C., Bony, S., & Dufresne, J.-L. (2014). Spread in model climate sensitivity traced to atmospheric convective mixing. *Nature*, 505(7481), 37–42. <https://doi.org/10.1038/nature12829>
- Siebesma, A. P., Soares, P. M. M., & Teixeira, J. (2007). A combined eddy-diffusivity mass-flux approach for the convective boundary layer. *Journal of the Atmospheric Sciences*, 64(4), 1230–1248. <https://doi.org/10.1175/JAS3888.1>
- Soares, P. M. M., Miranda, P. M. A., Siebesma, A. P., & Teixeira, J. (2004). An eddy-diffusivity/mass-flux parametrization for dry and shallow cumulus convection. *Quarterly Journal of the Royal Meteorological Society*, 130(604), 3365–3383. <https://doi.org/10.1256/qj.03.223>
- Sommeria, G., & Deardorff, J. W. (1977). Subgrid-scale condensation in models of nonprecipitating clouds. *Journal of the Atmospheric Sciences*, 34(2), 344–355. [https://doi.org/10.1175/1520-0469\(1977\)034<0344:sscimo>2.0.co;2](https://doi.org/10.1175/1520-0469(1977)034<0344:sscimo>2.0.co;2)
- Stephan, C. C., Schnitt, S., Schulz, H., Bellenger, H., de Szoeke, S. P., Acquistapace, C., et al. (2021). Ship- and island-based atmospheric soundings from the 2020 EUREC4A field campaign. *Earth System Science Data*, 13(2), 491–514. <https://doi.org/10.5194/essd-13-491-2021>
- Stevens, B., Bony, S., Brogniez, H., Hentgen, L., Hohenegger, C., Kiemle, C., et al. (2020). Sugar, gravel, fish and flowers: Mesoscale cloud patterns in the trade winds. *Quarterly Journal of the Royal Meteorological Society*, 146(726), 141–152. <https://doi.org/10.1002/qj.3662>
- Stevens, B., Bony, S., Farrell, D., Ament, F., Blyth, A., Fairall, C., et al. (2021). EUREC4A. *Earth System Science Data*, 13(8), 4067–4119. <https://doi.org/10.5194/essd-13-4067-2021>
- Suselj, K., Kurowski, M. J., & Teixeira, J. (2019a). On the factors controlling the development of shallow convection in eddy-diffusivity/mass-flux models. *Journal of the Atmospheric Sciences*, 76(2), 433–456. <https://doi.org/10.1175/JAS-D-18-0121.1>
- Suselj, K., Kurowski, M. J., & Teixeira, J. (2019b). A unified eddy-diffusivity/mass-flux approach for modeling atmospheric convection. *Journal of the Atmospheric Sciences*, 76(8), 2505–2537. <https://doi.org/10.1175/JAS-D-18-0239.1>
- Tan, Z., Kaul, C. M., Pressel, K. G., Cohen, Y., Schneider, T., & Teixeira, J. (2018). An extended eddy-diffusivity mass-flux scheme for unified representation of subgrid-scale turbulence and convection. *Journal of Advances in Modeling Earth Systems*, 10(3), 770–800. <https://doi.org/10.1002/2017MS001162>
- Vial, J., Bony, S., Stevens, B., & Vogel, R. (2017). Mechanisms and model diversity of trade-wind shallow cumulus cloud feedbacks: A review. *Surveys in Geophysics*, 38(6), 1331–1353. <https://doi.org/10.1007/s10712-017-9418-2>

- Vogel, R., Albright, A. L., Vial, J., George, G., Stevens, B., & Bony, S. (2022). Strong cloud circulation coupling explains weak trade cumulus feedback. *Nature*, 612(7941), 696–700. <https://doi.org/10.1038/s41586-022-05364-y>
- Vogel, R., Nuijens, L., & Stevens, B. (2020). Influence of deepening and mesoscale organization of shallow convection on stratiform cloudiness in the downstream trades. *Quarterly Journal of the Royal Meteorological Society*, 146(726), 174–185. <https://doi.org/10.1002/qj.3664>
- Wyngaard, J. C. (2004). Toward numerical modeling in the terra incognita. *Journal of the Atmospheric Sciences*, 61(14), 1816–1826. [https://doi.org/10.1175/1520-0469\(2004\)061<1816:TNMITT>2.0.CO;2](https://doi.org/10.1175/1520-0469(2004)061<1816:TNMITT>2.0.CO;2)
- Xiao, H., Ovchinnikov, M., Berg, L. K., & Mülmenstädt, J. (2023). Evaluating shallow convection parameterization assumptions with a q–w Quadrant analysis. *Journal of Advances in Modeling Earth Systems*, 15(8), e2022MS003526. <https://doi.org/10.1029/2022MS003526>
- Yu, X., & Lee, T.-Y. (2010). Role of convective parameterization in simulations of a convection band at grey-zone resolutions. *Tellus*, 62(5), 617–632. <https://doi.org/10.1111/j.1600-0870.2010.00470>
- Zhao, G., & Di Girolamo, L. (2006). Cloud fraction errors for trade wind cumuli from EOS-Terra instruments. *Geophysical Research Letters*, 33(20). <https://doi.org/10.1029/2006GL027088>